by positive staining with several monoclonal antibodies, i.e., RM-4 (Cosmo Bio Co., Ltd.) for macrophages, MRC OX-8 (mouse anti-rat CD8 alpha mAb, Serotec) for nonhelper T cells, and MRC OX-35 (mouse anti-rat CD4 mAb, Serotec) for helper T cells. The epithelioid cells and macrophages found around epithelioid cell granulomas were determined by positive staining with RM-4 (Fig. 2c). T cell subsets were characterized using MRC OX-35 and MRC OX-8.

The formalin-fixed, paraffin-embedded tumor and granuloma tissues were sectioned at 3 μm thickness and stained with hematoxylin and eosin (HE), whereas the frozen granuloma tissues were cut at 4 μm thickness. Immunohistochemical staining was carried out according to a standard immunostaining procedure [7–9]. Briefly, after deparaffization and rehydration (for MRC OX-6, MRC OX-8, and RM-4 mAbs), tissue sections were heated at 121°C for 15 min in 10 mM sodium citrate buffer, pH 6.0, for antigen retrieval (MRC OX-6 mAb). Frozen sections were fixed in ethanol (for MRC OX-3, MRC OX-17, and MRC OX-35 mAbs). Endogenous peroxidase activity was blocked for 5 min in methanol containing 3% hydrogen peroxide. Thereafter, slides were incubated with primary antibodies for 30 min at room temperature. The bound antibody was visualized by the avidin/biotin conjugate immunoperoxidase procedure using the HISTOFINE SAB 2 system HRP (Dako, Japan) and 3,3′-diaminobenzidine tetrahydrochloride (DAB) (Dako, Japan). Counterstaining was performed with hematoxylin.

PET imaging

PET experiments were performed in rats bearing BCG granulomas or KDH-8 tumors before (control) and after a prednisolone treatment. Eighteen days after BCG inoculation or 13 days after KDH-8 inoculation, the rats (n=3 for BCG granulomas and KDH-8 tumors, respectively) were fasted overnight, and anesthetized with pentobarbital (50 mg/kg body weight, i.p.). The rats were placed in a PET scanner (SHR-7700L, Hamamatsu Photonics, Hamamatsu, Japan) in a supine position and injected with FDG (28–30 MBq/rat) in the lateral tail vein. Sixty minutes after the injection of FDG, the rats underwent a first PET scanning for 15 min. After the PET scanning, the rats were treated with methylprednisolone acetate (8 mg/kg body weight). Twenty hours after the prednisolone treatment, a second FDG-PET scan was carried out using the same procedures as the first PET scan. The PET images were reconstructed by a standard filtered back-projection using a Hamming filter into a 256 × 256 × 31 (0.6 × 0.6 × 3.6 mm) matrix. The spatial resolution of the reconstructed images was 2.7 mm in the plane [10].

Statistical analysis

All values are expressed as mean ± standard deviation. To evaluate the significance of the differences in the values obtained between the control group and the treated group, an unpaired student's t test was performed.

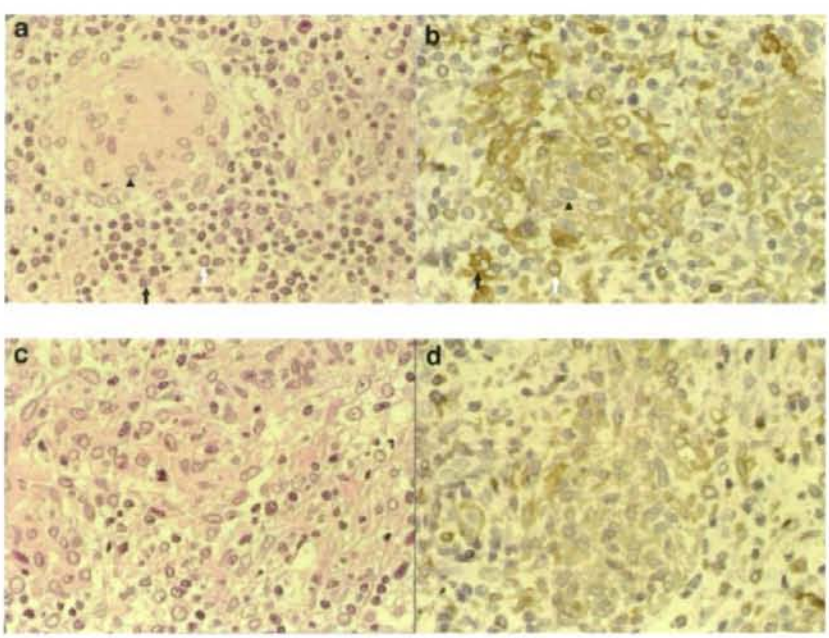

Fig. 1 Microscopic images (x 400) of HE-stained (**a**, **c**) and immunostained granuloma (**b**, **d**) for Ia antigen with MRC OX-6 mAb in control (**a**, **b**) and pretreated rats (**c**, **d**). **a** Mature epithelioid cell granuloma-formation and massive lymphocyte-infiltration. **b** Infiltrations of Ia-positive epithelioid cells and macrophages in granuloma and Ia-positive lymphocytes in granuloma periphery (for MRC OX-6). **c** Reduction of epithelioid cell granuloma-formation and lymphocyte-infiltration. **d** Reduction of infiltrations of Ia+ macrophages and Ia+ lymphocytes around granuloma. *Black arrow head* indicates epithelioid cell granuloma; *black arrow*, macrophage infiltration; *white arrow*, lymphocyte infiltration

A two-tailed value of $P<0.05$ was considered significant. The statistical program Stat View 5.0 was used for the data assessment.

Results

Histopathological findings

In the control animals inoculated with BCG, mature epithelioid cell granuloma-formation and massive lymphocyte-infiltration were observed in the calf muscle (Fig. 1a). Immunohistochemical staining with the MRC OX-6 mAb showed the accumulation of Ia^+ macrophages and Ia^+ lymphocytes into the periphery of the granuloma (Fig. 1b). In the prednisolone pretreatment group, reduction in the levels of epithelioid cell granuloma-formation and lymphocyte-infiltration and in the levels of Ia^+ macrophage-infiltration and Ia^+ lymphocyte-infiltration were observed (Fig. 1c and d). Immunostaining with MRC OX-3 and MRC OX-17 mAbs also showed the accumulation of Ia+ macrophages and Ia+ lymphocytes into the periphery of the granulomas in the control animals (Fig. 2a and b).

The different cell types in the granulomatous tissues were characterized by positive staining with several monoclonal antibodies. The epithelioid cells and macrophages determined by positive staining with RM-4 were found in the epithelioid cell granulomas and around epithelioid cell granulomas (Fig. 2c). Immunohistochemical staining of CD4 and CD8 showed numerous CD4+ (helper T cells) and CD8+ T cells (nonhelper T cells) surrounding the granulomas (Fig. 2d and e).

In the control animals inoculated with KDH-8, massive viable and proliferating cancer cells were observed by HE staining (Fig. 3a). Immunohistochemical staining with the MRC OX-6 mAb showed scattered Ia^+ macrophages-infiltration and Ia^+ lymphocytes-infiltration into the viable tumor cells (Fig. 3b). There were no histopathological changes for tumor tissue after treatment with prednisolone (Fig. 3c and d).

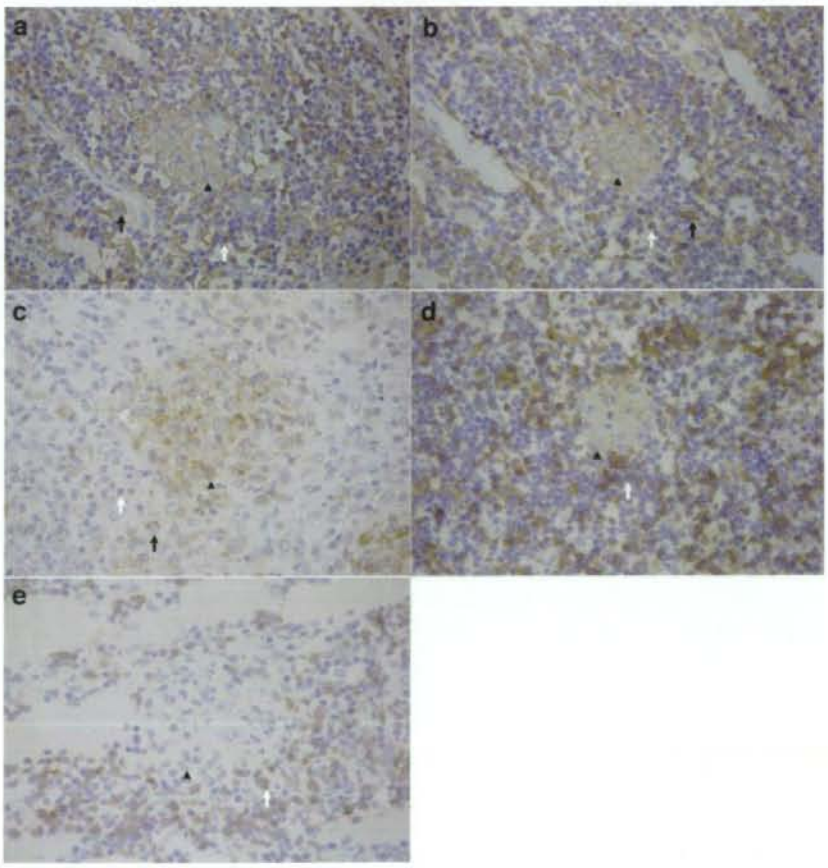

Fig. 2 Microscopic images (x 400) of immunostained for Ia antigen with MRC OX-3 (**a**), MRC OX-17 mAbs (**b**), and cell type characterization (**c-e**) in granulomas of control rats. **a** Accumulation of Ia+ epithelioid cells, Ia+ macrophages and Ia+ lymphocytes were characterized by MRC OX-3 mAb. **b** Accumulation of Ia+ epithelioid cells, Ia+ macrophages, and Ia+ lymphocytes were characterized by MRC OX-17 mAb. **c** The epithelioid cells and macrophages were determined by RM-4 positive staining. **d** CD4+ T cells (helper T cells) were determined by MRC OX-35 mAb. **e** CD8+ T cells (nonhelper T cells) were determined by MRC OX-8 mAb. *Black arrow head* indicates epithelioid cell granuloma; *black arrow*, macrophage infiltration; *white arrow*, lymphocyte infiltration

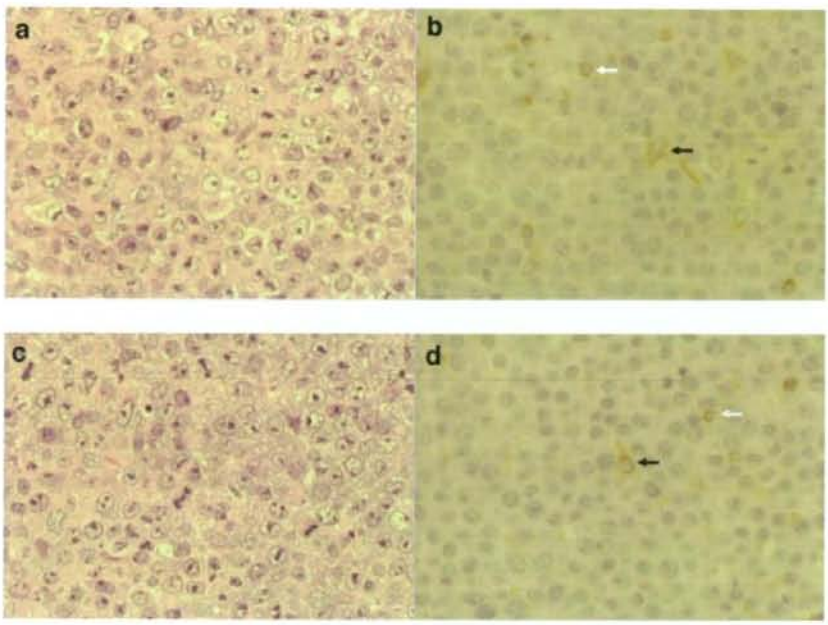

Fig. 3 Microscopic images (× 400) of HE-staining (**a**, **c**) and immunostaining with MRC OX-6 mAb for Ia antigen (**b**, **d**) in the control (**a**, **b**) and pretreated (**c**, **d**) rats bearing KDH-8 tumors. No pathological changes were observed in the tumor tissues between the untreated (control) and prednisolone-treated groups. *Black arrow* indicates macrophage infiltration; *white arrow*, lymphocyte infiltration

Uptake of FDG

FDG uptakes in the granuloma and tumor are summarized in Table 1 and Fig. 4. In the control groups, the level of FDG uptake in the granuloma was 0.909±0.142 (%ID/g) x kg which was comparable to that in the hepatoma (0.929× 0.164 (%ID/g) x kg). There was no significant difference in the level of FDG uptake between the granuloma and the tumor tissues (P=NS).

Prednisolone pretreatment significantly decreased the level of FDG uptake in the granuloma to 52% of the control value (P<0.001), while that in the tumor did not decrease significantly (85% of the control value; P=NS). The uptake levels of FDG in the granuloma and tumor tissues in the prednisolone pretreated group were 0.477± 0.139 and 0.788±0.080 (%ID/g) x kg, respectively, and the difference was significant (P<0.01) (Fig. 4).

The granuloma-to-muscle (L/M) and the granuloma-to-blood (L/B) ratios of FDG uptake were 33.5±9.7 and 9.4± 1.9 in the control group, respectively. Both the L/M ratio and L/B ratio of FDG uptake of the granuloma in the prednisolone pretreated group were significantly lower (14.4±4.0, P<0.01 for L/M ratio and 6.0±1.8, P<0.05 for L/B ratio) than those in the control group. Both the L/M ratio and L/B ratio of FDG uptake of the tumor were not significantly affected by the prednisolone pretreatment (Table 1).

Table 1 FDG uptake in granuloma and tumor

FDG uptake ((%ID/g) × kg)	Granuloma		Tumor	
	Control (n=5)	Steroid (n=6)	Control (n=6)	Steroid (n=5)
Granuloma or tumor	0.909±0.142	0.477±0.139**	0.929±0.164	0.788±0.080
Muscle	0.028±0.005	0.033±0.003	0.025±0.011	0.027±0.006
Blood	0.098±0.006	0.080±0.007**	0.060±0.017	0.054±0.015
L/M ratio	33.5±9.7	14.4±4.0**	41.0±10.9	29.6±6.0
L/B ratio	9.4±1.9	6.0±1.8*	15.9±2.4	15.3±3.2

L/M ratio, lesion (granuloma or tumor)-to-muscle ratio of FDG uptake
L/B ratio, lesion (granuloma or tumor)-to-blood ratio of FDG uptake
Control, control group; Steroid, prednisolone (PRE)-pretreated group
Data are mean±SD
*P<0.05, **P<0.01 compared with control group

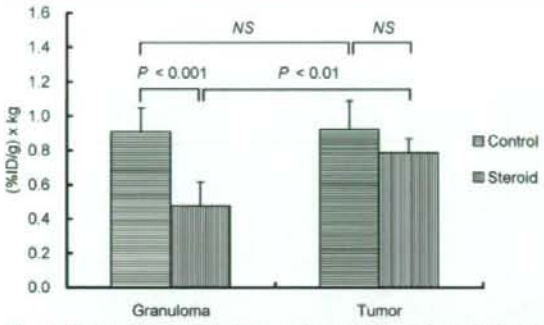

Fig. 4 FDG uptake in granuloma and tumor tissues in control and prednisolone pretreated groups. *Control* indicates the control group; *steroid* prednisolone (PRE)-pretreated group. *NS* is not statistically significant. Values given are mean ± SD

Blood glucose level and lesion weight

The blood glucose levels showed consistent tendency to increase by prednisolone pretreatment with a significant difference between the control and the pretreated rats bearing tumors (87.3±11.1 mg/dl vs 124.8±11.7 mg/dl at the time of FDG intravenous injection, $P<0.05$) (Table 2). The granuloma weight was significantly reduced by the prednisolone pretreatment (0.137±0.027 g for control rats and 0.089±0.024 g for pretreated rats, $P<0.05$), while the tumor weight was not (4.435±1.806 g for control rats and 4.085±2.083 g for pretreated rats, P=NS). There were no significant differences in the body weight of rats among all groups (Table 2).

PET images

Figure 5 shows representative FDG-PET images of rats bearing BCG granulomas or KDH-8 tumors before and after a prednisolone treatment. BCG granulomas and tumors were clearly visualized before the prednisolone treatment (Fig. 5a and c, control). Prednisolone treatment markedly reduced the uptake of FDG in BCG granulomas (Fig. 5b), but not in tumors (Fig. 5d).

Discussion

In this study, we developed an intramuscular granuloma rat model characterized by epithelioid cell granuloma-formation and massive lymphocyte-infiltration around the granuloma (Fig. 1a and b), histologically similar to those observed in sarcoidosis [11]. The granuloma showed high FDG uptake comparable to that of the tumor (Figs. 4 and 5). In addition, the present study demonstrated that the effect of prednisolone pretreatment on FDG uptake was greater in the granulomatous lesions than that in the tumor (Figs. 4 and 5). These results suggest that BCG-induced granuloma may be a valuable model and may provide a biological basis for FDG studies.

In our model, extensive FDG uptake was observed in the granuloma, which was comparable to that in the tumor. To the best of our knowledge, there have been no studies showing a comparison of FDG uptake in experimental granulomas and tumors, although increased FDG uptake in inflammatory lesions has been reported in experimental inflammation induced by an intramuscular injection of *S. aureus* or turpentine oil [5, 6]. In our previous study, the inflammatory lesions induced by *S. aureus* and turpentine oil showed levels of FDG uptake which were about 45% and 34% of that in KDH-8 tumor, respectively [6]. van Waarde et al. also suggested that FDG uptake in the turpentine oil-induced inflammatory lesion was about 35% of that in C6 rat glioma [5]. *S. aureus* and turpentine-induced inflammatory tissues showed massive neutrophil-infiltration and ambient connective tissue-formation around the injection sites of *S. aureus* and turpentine oil. Increased FDG distribution was mainly shown in the areas of neutrophil-infiltration, and FDG distribution was lower in the ambient connective tissues. On the contrary, in our granuloma model, increased FDG distribution was mainly shown in the epithelioid cell granulomas by our preliminary experiments using autoradiography (data not shown). The activities of granuloma formation and granuloma-associated immune cells may be reflected by FDG accumulation, although detailed mechanisms of the accumulation occur-

Table 2 Blood glucose level and body and lesions weights

		Granuloma		Tumor	
	Parameter	Control (n=5)	Steroid (n=6)	Control (n=6)	Steroid (n=5)
Blood glucose (mg/dl)	0 min	87.0±9.3	95.7±8.3	87.3±11.1	124.8±11.7*
	60 min	79.6±6.6	87.0±10.0	86.7±8.8	96.8±11.4
	Body weight (kg)	0.270±0.015	0.260±0.013	0.235±0.030	0.239±0.029
	Lesion weight (g)	0.137±0.027	0.089±0.024*	4.435±1.806	4.085±2.083

0 min at FDG injection; 60 min at sacrifice; Control indicates the control group; steroid, the prednisolone (PRE)-pretreated group
Data are mean ± SD
*$P<0.05$ compared with control group

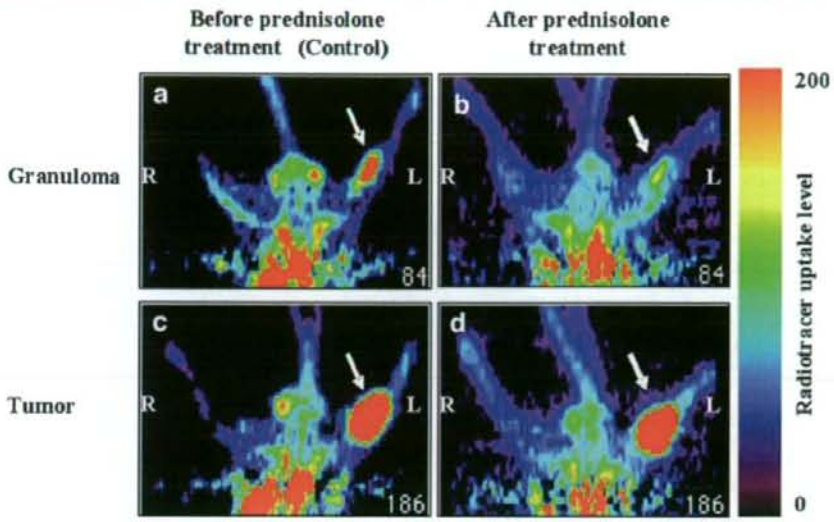

Fig. 5 FDG-PET images of rats bearing BCG granulomas (**a** and **b**) or KDH-8 tumors (**c** and **d**). Horizontal PET images before (**a** and **c**) and after prednisolone treatment (**b** and **d**) are shown. *Arrows* indicate the locations of BCG granulomas (**a** and **b**) and KDH-8 tumors (**c** and **d**) inoculated in the left calf muscles of rats. Color scale depicts radiotracer uptake level normalized to animal body weight and injected dose. *R* indicates right; *L*, left

ring in the granuloma remain unclarified. The animal models of inflammation induced by *S. aureus* and turpentine oil may not be suitable models for differentiating malignant tumors from benign diseases because of the relatively low FDG uptake levels in their inflammatory lesions. In contrast, our granuloma rat model showed a high FDG uptake in the granulomatous lesions comparable to that in the KDH-8 tumor, indicating the suitability of our model for such studies.

Our intramuscular granuloma rat model showed histologically similar characteristics to sarcoidosis [11, 12], as shown in Figs. 1 and 2. Sarcoidosis is a main source of false-positive FDG-PET findings in oncology. Sarcoidosis can be characterized in the affected organs by an accumulation of activated macrophages (epithelioid cells and multinuclear giant cells) and activated T lymphocytes at the site of disease activity. Pathologically, the first manifestation of the disease is an accumulation of mononuclear inflammatory cells, mainly CD4+ T helper 1 lymphocytes and mononuclear phagocytes in the affected organ. This inflammatory process is followed by the formation of granulomas, and aggregations of macrophages and their progeny, epithelioid cells, and multinucleated giant cells [13, 14]. This study showed the accumulation of epithelioid cells and macrophages defined by positive staining with RM-4 (Fig. 2c) in the granuloma, and CD4+ lymphocytes into the periphery of the granuloma (Fig. 2d), indicating the histological similarity of our model to sarcoidosis [9]. The cellular uptake of FDG in sarcoidosis is considered to be related to its inflammatory cell infiltrates, which are composed of lymphocytes, macrophages, and epithelioid cells from monocytes, because FDG has been observed in vitro to be accumulated by leukocytes [15, 16], lymphocytes, and macrophages [17]. The histological similarity of our granuloma rat model to sarcoidosis indicates its potential for providing a biological basis for differentiating sarcoidosis from malignant tumors, although detailed investigations, including those on FDG distribution at the cellular level, are required.

The immune-associated (Ia) antigen represents a 23,000- and 30,000-dalton membrane glycoprotein complex. The Ia antigen is normally expressed on all B-lymphocytes and some monocytes, but not in large amounts on normal T cells unless they are activated by allogenic or mitogenic stimulation [18]. The expression of Ia antigen on T cells is a sign of T cell activation in active sarcoidosis [19]. The present study also showed the accumulation of Ia positive (Ia^+) epithelioid cells and macrophages in the granuloma and Ia^+ lymphocytes into the periphery of the granuloma (Figs. 1, 2a and b), which further support the histological similarity of our model to sarcoidosis [9]. The extensive FDG uptake in the granuloma was decreased by prednisolone pretreatment, being concordant with the reduction in epithelioid cell granuloma-formation and lymphocyte-infiltration, including the infiltrations of Ia^+ macrophages and Ia^+ lymphocytes (Figs. 1c and d, 4b). These results suggest that FDG uptake might reflect active granulomatous processes.

For almost four decades, oral corticosteroids have been the mainstay of treatment in pulmonary sarcoidosis [20, 21]. To elucidate the mechanism of glucocorticoid on the suppressive course of the reaction to granulomatous lung tissue in experimental pulmonary granulomas, Gemma et al. [8] have performed immunohistochemical staining of an Ia+ antigen at 1 and 2 days after high-dose prednisolone treatment. The results showed a remarkable reduction in the number of Ia+ macrophages and Ia+ lymphocytes in the granulomatous lung tissue after the treatment with prednis-

olone. These findings suggest that glucocorticoid may suppress the immunological activities of macrophages and T cells through their inhibitory effect on the differentiation of Ia+ macrophages and activated T cells, which may result in the diminishment of the pulmonary granulomatous reaction through the disorder of the macrophage-T cell interaction. In patients with pulmonary sarcoidosis, FDG uptake in the lung was decreased after high-dose steroid therapy concordant with the histologic activity in the lung [2, 3, 14]. The present study showed that prednisolone pretreatment significantly decreased the level of FDG uptake in the granuloma to 52% of the control value (Table 1, Fig. 4). Our histological findings showed that the Ia^+ macrophage-infiltration, epithelioid cell granuloma-formation, and activated T lymphocyte-infiltration in the granuloma were decreased by prednisolone pretreatment. The decreased FDG uptake in the granuloma by the steroid pretreatment may be ascribed to the reduced histologic activity, including epithelioid cell granuloma-formation and lymphocyte-infiltration. The current results are in accordance with those in patients with pulmonary sarcoidosis [2, 3, 19]. On the other hand, the level of FDG uptake and histological features of the tumor were not significantly affected by the prednisolone pretreatment. Taken together, corticosteroid pretreatment may provide a potential means for differentiating malignant tumors from granulomatous lesions in FDG-PET studies, although further studies in other animal models and in patients are needed to confirm the present results.

In this study, to generate experimental tumors, allogenic hepatoma cells (KDH-8) were inoculated into the left calf muscle of rats. The histopathological characterization of intramuscular tumor tissues showed massive viable and proliferating cancer cells by HE staining and few Ia+ macrophage-infiltration and Ia+ lymphocyte-infiltration defined by the MRC OX-6 mAb into viable tumor cells 14 days after the inoculation of KDH-8. However, the inflammatory cells could seldom be seen around the tumor graft by HE and immunohistochemical stains. Hashimoto et al. [22] have also reported that the lesion consisted of many viable tumor cells with few tumor-tissue infiltrating lymphocytes in the tumor and several granulocytes and macrophages at the center of the tumor bearing into the leg muscle of WKAH rats 14 days after inoculation of KDH-8. In the present study, FDG uptake level in the tumor was decreased slightly after prednisolone treatment, although the difference was not significant (85% of the control value). On the other hand, there were no obvious histopathological changes in the tumor tissue after prednisolone treatment (Fig. 3c and d). Accordingly, the anti-inflammatory/immune effects of prednisolone may not be responsible for the reduction in tumoral FDG uptake level. Elevated blood glucose levels induced by corticosteroid and the antitumoral effects of prednisolone may be other explanations for the reduction in the tumoral FDG uptake level.

In the present study, the blood glucose levels showed consistent tendency to increase by the prednisolone pretreatment with a significant difference between the control and pretreated rats bearing tumor. It is well known that the action of steroids on glucose metabolism increases the blood glucose level [23, 24]. The uptake of FDG in tissues is affected by the blood glucose level [25, 26]. Accordingly, the reduced FDG uptake in the granuloma and tumor may be partly ascribed to the elevated blood glucose levels. However, the effect of prednisolone pretreatment on FDG uptake was greater in the granuloma than in the tumor, although the elevation in the blood glucose level was higher in rats bearing tumor. A slight elevation in the blood glucose level (125 mg/dl) following PRE pretreatment may not affect the uptake levels of FDG in the tumor, as reported previously [5, 27]. Detailed investigations, including quantitative evaluation of inflammation levels (i.e., determination of inflammatory cell density) and autoradiographic studies using FDG, are required to clarify the reason for the reduction in tumoral FDG uptake level.

As mentioned above, it is of great importance to clarify the detailed FDG distribution at the cellular level in the granuloma. In this regard, Kubota et al. reported a high FDG accumulation in young granulation tissues around the tumor and in the macrophages infiltrating the marginal areas surrounding the extensive tumor necrosis by micro-autoradiographies of FDG and ^{3}H-DG [17]. Activated inflammatory cells have markedly increased glycolysis. The hexose monophosphate shunt is stimulated by phagocytosis, which is enhanced 20–30-fold that of baseline values which is the cause of the high FDG uptake [28]. Although microautoradiographic studies of ^{3}H-FDG or ^{14}C-FDG are needed to clarify the detailed FDG distribution at the cellular level in our granuloma rat model, the results of this study indicate that a high FDG uptake in the granuloma is related to the activation of inflammatory cell infiltrates, including mature epithelioid cells, massive macrophages, and lymphocytes.

The PET images showed that BCG granuloma and tumors were clearly visualized before the prednisolone treatment (Fig. 5a and c, control). Prednisolone treatment markedly reduced FDG uptake in BCG granulomas but not in tumors (Fig. 5b and d). These results demonstrate that PET is a useful noninvasive imaging method to depict and assess early changes in FDG uptake by the corticosteroid treatment.

Low-grade hepatocellular carcinoma (HCC) has a low FDG uptake level due to its histological characteristics of being closer to the normal liver, which has abundant glucose-6-phophatase. However, high-grade HCC, intra-

and extrahepatic metastases, and distant metastases correlated with positivity of FDG-PET. Thus, FDG-PET imaging has a clinically significant impact on the management of patients diagnosed with HCC [29]. KDH-8 is a rat transplantable hepatocellular carcinoma that is found in WKAH rats and is histologically poorly undifferentiated. Our previous study showed that the FDG uptake level in the hepatoma was the same as or higher than that in the other tumor models [5]. Our hepatoma model, employed as an extrahepatic metastase, should provide a biological basis for evaluating the impact of FDG imaging on the management of patients diagnosed with hepatocellular carcinoma.

It should be noted that there are several limitations to our study. First, each rat was inoculated with BCG granulomas or KDH-8 tumors in this study because FDG uptake may be affected if both the BCG granulomas and the KDH-8 tumors were inoculated into the same rat. However, it is possible to inject BCG and KDH-8 cells in the same animal, and a rat model bearing both the BCG granulomas and the KDH-8 tumors may be useful to determine the differences in FDG uptake profiles between the granulomas and tumors. Second, anesthesia may affect FDG uptake, as the rats were kept under pentobarbital anesthesia during FDG uptake. In this regard, Lee et al. have reported that pentobarbital injection elevated blood FDG activity to 2.0-fold higher than the control levels, but had no effect on tumor uptake [30]. Recently, we compared the effects of pentobarbital and ketamine/medetomidine on FDG uptake in a rat model bearing KDH-8 tumors. The results showed no change in FDG uptake levels for either anesthetic agent. The effects of anesthesia on FDG uptake in tumors appeared to be small, compared with those in the brain. Finally, it is important to quantify the level of inflammation for FDG uptake correlation studies. Unfortunately, we could not perform quantitative evaluation of inflammation levels, which prevented us to accurately evaluate the correlation between the level of inflammation and FDG uptake level in the tumors and granulomas. Although our findings show that the pathological characterization of the BCG granulomas was similar to that of sarcoidosis, and FDG accumulation level was decreased by steroid treatment, detailed investigations, including quantitative evaluation of inflammation levels (i.e., determination of inflammatory cell density) and autoradiographic studies using FDG, are required to accurately evaluate the correlation between the level of inflammation and FDG distribution.

Conclusion

In the present study, we developed a BCG-induced granuloma rat model which has similar histopathological features as those of sarcoidosis. The granuloma showed a high FDG uptake comparable to that of the tumor. In addition, our results demonstrate that the effect of prednisolone pretreatment on FDG uptake was greater in the granuloma than in the tumor. These results suggest the usefulness of our model for studying FDG accumulation in inflammatory lesions.

Acknowledgments This work was supported in part by a grant-in-aid for Scientific Research from the Japan Society for the Promotion of Science, by a grant-in-aid for Scientific Research from the Japanese Ministry of Education, Culture, Sports, Science and Technology, by Special Coordination Funds for Promoting Science and Technology provided by the Ministry of Education, Culture, Sports, Science and Technology, the Japanese Government, by a Grant-in-Aid for Cancer Research from the Ministry of Health and Welfare of Japan, and by a grant from the Rotary Yoneyama Memorial Foundation, Inc. The authors are grateful to the staff members of the Department of Nuclear Medicine, Central Institute of Isotope Science and Institute for Animal Experimentation, Hokkaido University and the Facility of Radiology, Hokkaido University Hospital, for supporting this study. We also thank Eriko Suzuki, secretary of the professor of the Department of Nuclear Medicine, Hokkaido University, for continuously supporting this study and Makoto Sato, SHI Accelerator Service Ltd., for FDG syntheses.

References

1. Dimitrakopoulou-Strauss A, Strauss LG, Heichel T, Wu H, Burger C, Bernd L, et al. The role of quantitative (18)F-FDG PET studies for the differentiation of malignant and benign bone lesions. J Nucl Med 2002;43:510–8.
2. Brudin LH, Valind S, Rhodes CG, Pantin CF, Sweatman M, Jones T, et al. Fluorine-18 deoxyglucose uptake in sarcoidosis measured with positron emission tomography. Eur J Nucl Med 1994;21:297–305.
3. Lewis PJ, Salama A. Uptake of fluorine-18-fluorodeoxyglucose in sarcoidosis. J Nucl Med 1994;35:1647–9.
4. Ohtsuka T, Nomori H, Watanabe K, Naruke T, Orikasa H, Yamazaki K, et al. False-positive findings on [18F]FDG-PET caused by non-neoplastic cellular elements after neoadjuvant chemoradiotherapy for non-small cell lung cancer. Jpn J Clin Oncol 2005;35:271–3.
5. van Waarde A, Cobben DC, Suurmeijer AJ, Maas B, Vaalburg W, de Vries EF, et al. Selectivity of 18F-FLT and FDG for differentiating tumor from inflammation in a rodent model. J Nucl Med 2004;45:695–700.
6. Zhao S, Kuge Y, Tsukamoto E, Mochizuki T, Kato T, Hikosaka K, et al. Effects of insulin and glucose loading on FDG uptake in experimental malignant tumours and inflammatory lesions. Eur J Nucl Med 2001;28:730–5.
7. Zhao S, Kuge Y, Mochizuki T, Takahashi T, Nakada K, Sato M, et al. Biologic correlates of intratumoral heterogeneity in FDG distribution with regional expression of glucose transporters and hexokinase-II in experimental tumor. J Nucl Med 2005;46:675–82.
8. Gemma H, Sato A. Effect of glucocorticoid on lung tissue and bronchus-associated lymphoid tissue of experimental granulomatous lung. Kekkaku 1989;64:387–99.
9. Whiteland JL, Nicholls SM, Shimeld C, Easty DL, Williams NA, Hill TJ. Immunohistochemical detection of T-cell subsets

and other leukocytes in paraffin-embedded rat and mouse tissues with monoclonal antibodies. J Histochem Cytochem 1995;43: 313–20.
10. Watanabe M, Okada H, Shimizu K, Omura T, Yoshikawa E, Kosugi T, et al. A high resolution animal PET scanner using compact PS-PMT detectors. IEEE Trans Nucl Sci 1997;44:1277–82.
11. Schrier DJ, Ripani LM, Katzenstein AL, Moore VL. Role of angiotensin-converting enzyme in bacille Calmette-Guerin-induced granulomatous inflammation. Increased angiotensin-converting enzyme levels in lung lavage and suppression of inflammation with captopril. J Clin Invest 1982;69:651–7.
12. Sandor M, Weinstock JV, Wynn TA. Granulomas in schistosome and mycobacterial infections: a model of local immune responses. Trends Immunol 2003;24:44–52.
13. Chang JM, Lee HJ, Goo JM, Lee HY, Lee JJ, Chung JK, et al. False positive and false negative FDG-PET scans in various thoracic diseases. Korean J Radiol 2006;7:57–69.
14. du Bois RM. Corticosteroids in sarcoidosis: friend or foe? Eur Respir J 1994;7:1203–9.
15. Osman S, Danpure HJ. The use of 2-[18F]fluoro-2-deoxy-D-glucose as a potential in vitro agent for labeling human granulocytes for clinical studies by positron emission tomography. Int J Rad Appl Instrum B 1992;19:183–90.
16. Borregaard N, Herlin T. Energy metabolism of human neutrophils during phagocytosis. J Clin Invest 1982;70:550–7.
17. Kubota R, Yamada S, Kubota K, Ishiwata K, Tamahashi N, Ido T. Intratumoral distribution of fluorine-18-fluorodeoxyglucose in vivo: high accumulation in macrophages and granulation tissues studied by microautoradiography. J Nucl Med 1992;33:1972–80.
18. Winchester RJ, Kunkel HG. The human Ia system. Adv Immunol 1979;28:221–92.
19. Costabel U, Bross KJ, Ruhle KH, Lohr GW, Matthys H. Ia-like antigens on T-cells and their subpopulations in pulmonary sarcoidosis and in hypersensitivity pneumonitis. Analysis of bronchoalveolar and blood lymphocytes. Am Rev Respir Dis 1985;131:337–42.
20. Siltzbach LE. Effects of cortisone in sarcoidosis: a study of thirteen patients. Am J Med 1952;12:139–60.
21. Milman N. Oral and inhaled corticosteroids in the treatment of pulmonary sarcoidosis—a critical reappraisal. Sarcoidosis Vasc Diffuse Lung Dis 1998;15:150–7.
22. Hashimoto S, Shirato H, Hosokawa M, Nishioka T, Kuramitsu Y, Matushita K, et al. The suppression of metastases and the change in host immune response after low-dose total-body irradiation in tumor-bearing rats. Radiat Res 1999;151:717–24.
23. West KM. Comparison of the hyperglycemic effects of glucocorticoids in human beings; the effect of heredity on responses to glucocorticoids. Diabetes 1957;6:168–75.
24. Pellacani A, Fornengo P, Bruno A, Ceruti C, Mioletti S, Curto M, et al. Acute methylprednisolone administration induces a transient alteration of glucose tolerance and pyruvate dehydrogenase in humans. Eur J Clin Invest 1999;29:861–7.
25. Wahl RL, Henry CA, Ethier SP. Serum glucose: effects on tumor and normal tissue accumulation of 2-[F-18]-fluoro-2-deoxy-D-glucose in rodents with mammary carcinoma. Radiology 1992;183:643–7.
26. Lindholm P, Minn H, Leskinen-Kallio S, Bergman J, Ruotsalainen U, Joensuu H. Influence of the blood glucose concentration on FDG uptake in cancer—a PET study. J Nucl Med 1993;34:1–6.
27. Zhao S, Kuge Y, Nakada K, Mochizuki T, Takei T, Okada F, et al. Effect of steroids on [18F]fluorodeoxyglucose uptake in an experimental tumour model. Nucl Med Commun 2004;25:727–30.
28. Amrein PC, Larson SM, Wagner HN Jr. An automated system for measurement of leukocyte metabolism. J Nucl Med 1974; 15:352–5.
29. Wudel LJ Jr, Delbeke D, Morris D, Rice M, Washington MK, Shyr Y, et al. The role of [18F]fluorodeoxyglucose positron emission tomography imaging in the evaluation of hepatocellular carcinoma. Am Surg 2003; 69:117–24.
30. Lee KH, Ko BH, Paik JY, Jung KH, Choe YS, Choi Y, et. al. Effects of anesthetic agents and fasting duration on 18F-FDG biodistribution and insulin levels in tumor-bearing mice. J Nucl Med 2005;46:1531–6.

Luminescence 2007; 22: 455–461
Published online 4 July 2007 in Wiley InterScience (www.interscience.wiley.com) DOI: 10.1002/bio.984 *ORIGINAL RESEARCH*

Development of a novel neodymium compound for *in vivo* fluorescence imaging

Kazuki Aita, Takashi Temma, Yuji Kuge and Hideo Saji*

Department of Patho-functional Bioanalysis, Graduate School of Pharmaceutical Sciences, Kyoto University, Japan

Received 17 November 2006; revised 12 April 2007; accepted 12 April 2007

ABSTRACT: We developed a novel fluorescent probe that contains the neodymium(III) complex moiety and fluorescein moiety. This probe can emit long-lived near-infrared luminescence derived from a Nd ion through excitation of the fluorescein moiety with visible light (λ_{ex} = 488 nm, λ_{em} = 880 nm, lifetime = 2.3 μs). These results indicate the possibility of the probe as a candidate for *in vivo* fluorescence molecular imaging. Copyright © 2007 John Wiley & Sons, Ltd.

KEYWORDS: neodymium; near-infrared; fluorescein; energy transfer; long-lived luminescence

INTRODUCTION

Molecular imaging is a rapidly emerging biomedical research field that may be defined as the visual representation, characterization and quantification of biological processes at the cellular and subcellular levels within a living organism (1–3). As a technique of molecular imaging, fluorescence imaging attracts great interest.

In vivo fluorescence imaging, however, has several points that need to be considered, such as the permeability of the emission light, the background from scattered and reflected excitation light and self-fluorescence from tissues. To overcome such problems, the development of novel *in vivo* fluorescent probes has been required.

Near-infrared (NIR) light (700–1000 nm) has a potential for *in vivo* imaging. Provided that NIR light is used as emission light, it can permeate the body without intense absorbance and scatter by tissues (4) to offer a solution to problems such as permeability and background. In addition it has another advantage, that most biological compounds in living systems have no self-fluorescence in the NIR region.

Scattered and reflected light derived from excitation light are other obstacles, increasing background noise. Fortunately, background noise from excitation light can be removed by appropriate filters, provided that the difference between the excitation and emission wavelengths of the probe (Stoke's shift) is large enough; therefore, fluorescent probes with a large Stoke's shift have the potential to increase the S/N ratio in *in vivo* fluorescent imaging. However, most previously reported NIR probes (5–7) had an organic fluorescence centre with a small Stoke's shift ineffective for removing noise.

Consequently, we planned to develop a new fluorescent probe by chelating a neodymium (Nd) ion in its fluorescent centre for *in vivo* fluorescence imaging. Nd complexes have luminescence originating from $^4F_{3/2}$ to $^4I_{9/2}$ transition in the NIR region of 880 nm (8–10), unlike other lanthanide ions (e.g. Eu and Tb), and their Stoke's shift exceeds 200 nm, which is nearly 10 times larger than typical fluorescent dyes (fluorescein and rhodamine have Stoke's shifts of ~25 nm and ~20 nm, respectively). Such a favourable characteristic can increase the S/N ratio with the use of appropriate filters. In addition, the lifetime of lanthanide luminescence reaches the microsecond (μs) or millisecond (ms) order in contrast to the nanosecond (ns) order of organic fluorophores, making it possible to further cut down noise by time-resolved fluorescence imaging (4, 11).

As a chelating moiety, 1,4,7,10-tetraazacyclododecane-1,4,7,10-tetraacetic acid (DOTA) was selected, because DOTA and a Nd^{3+} ion form a highly stable complex [the log K value of Nd^{3+} and $DOTA^{4-}$ is 25.69 (12)] due to the tight coordination of DOTA with eight positions at maximum. This implies that the complex is not susceptible to metabolic degradation in living systems (13).

To excite a Nd ion, an antenna moiety, a sensitizing chromophore, is required in the structure because of the low absorbance of lanthanide f–f transitions (14). Thus, we selected fluorescein as the antenna moiety because of its long, less harmful excitation wavelength (~500 nm) and previous success in transferring energy to Nd (14). Moreover, it is also important that fluorescein is widely used in various fields, is highly soluble in water and can be easily modified for use in follow-up studies (15, 16).

*Correspondence to: H. Saji, Department of Patho-Functional Bioanalysis, Graduate School of Pharmaceutical Sciences, Kyoto University, Japan.
E-mail: hsaji@pharm.kyoto-u.ac.jp

Contract/grant sponsor: 21st Century COE Programme, Japan.

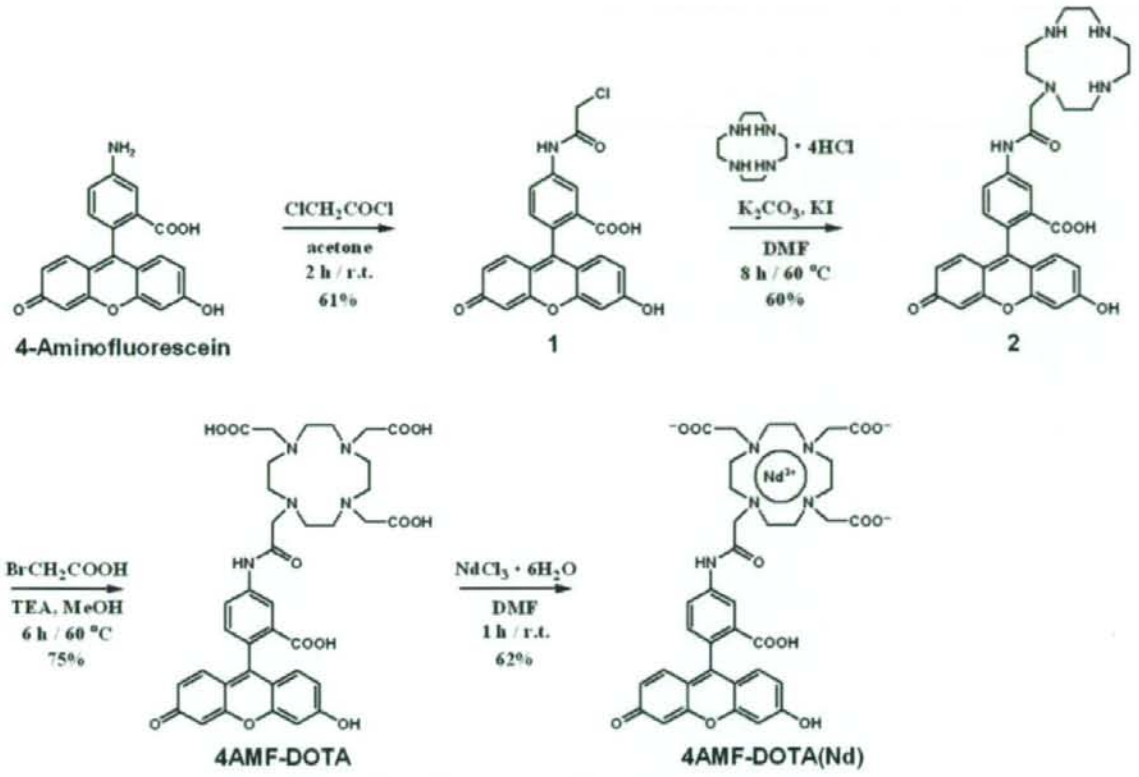

Scheme 1. Synthetic reaction scheme for 4AMF-DOTA(Nd).

In this study, we synthesized 4AMF-DOTA(Nd) including the Nd-DOTA (1,4,7,10-tetraazacyclododecane-1,4,7,10-triacetic acid) complex and fluorescein as a NIR fluorescent probe (Scheme 1), and investigated its chemical and physical features.

MATERIALS AND METHODS

Materials

All chemicals used in this study were commercial products of the highest purity and were further purified by standard methods if necessary.

Instruments

FT-IR spectra were recorded using a Jasco FT/IR-4100 (Nihon Bunko Inc., Tokyo, Japan). UV-vis spectra were measured using a Hitachi U2001 (Hitachi High-Tech Manufacturing & Service Corp., Ibaraki, Japan). Electrospray mass spectral (ESI–MS) measurements were performed on a SHIMADZU LC-MS2010 EV (Shimadzu Corp., Kyoto, Japan). ^{1}H-NMR spectra were recorded on a JEOL JNM-AL400 (JEOL Ltd, Tokyo, Japan). Fluorescence spectroscopy was performed with a Fluorolog-3 (Horiba Jobin Yvon Inc., Kyoto, Japan). The slit width was 10 nm for both excitation and emission. Time-resolved fluorescence spectra were recorded on a Fluorolog-3 with Phosphorescence (Horiba Jobin Yvon). The slit width was 12 nm for both excitation and emission. In both fluorescence spectra measurements, the photomultiplier voltage was 1450 V.

Fluorescence emission and excitation spectral measurements

The fluorescence emission spectra of 4AMF-DOTA(Nd) (10 μmol/L) without delay time were measured in 10 mmol/L Tris–HCl buffer, pH 8.0, 10 mmol/L Britton–Robinson buffer, pH 2–11, MeOH, EtOH and DMSO (each organic solvent contained 0.1% v/v Et_3N) at 25°C, following excitation at 488, 498, 504 and 523 nm in the buffers, MeOH, EtOH and DMSO, respectively. Excitation spectra were obtained at an emission wavelength of 870 nm.

Time-delayed luminescence spectral measurement

The time-delayed luminescence spectra of 4AMF-DOTA(Nd) (10 μmol/L) were measured in 10 mmol/L Tris–HCl buffer, pH 8.0, at 25°C, following excitation at 488 nm. A delay time of 7 μs and a gate time of 100 μs were used.

UV-visible absorption spectral measurement

The absorption spectral changes of 4AMF-DOTA(Nd) (10 μmol/L) in 10 mmol/L Tris–HCl buffer, pH 8.0, at 25°C were determined.

Luminescence lifetime measurements

The luminescence lifetime of 4AMF-DOTA(Nd) (10 μmol/L) in 10 mmol/L Tris–HCl buffer, pH 8.0, at 25°C was determined. Data were collected at 1 μs resolution and fitted to a single-exponential curve using the equation shown below, where I_0 and I are the luminescence intensities at time $t = 0$ and time t, respectively, and τ is the luminescence emission lifetime. Lifetime was obtained by monitoring emission intensity at 870 nm ($\lambda_{ex} = 488$ nm):

$$I = I_0 \exp(-t/\tau)$$

Synthesis

4-(Chloromethylamido)fluorescein (4AMF-Cl). 4-Aminofluorescein (1.0 g, 3.0 mmol) was dissolved in acetone (20 mL). To the solution was added $ClCH_2COCl$ (372 mg, 3.3 mmol) in acetone solution (10 mL). A yellow powder was formed instantly. The mixture was then stirred for 5 h at room temperature. The mixture was concentrated by evaporation and the resulting residue was redissolved in MeOH. The solution was poured into Et_2O (200 mL), and the resulting residue was washed with Et_2O by decantation three times. The powder was dried under vacuum to obtain 4AMF-Cl (852 mg, 1.9 mmol, 61%) as a yellow powder. MS (ESI, pos.), m/z found 425 ($[M+H]^+$), calcd. 425 ^{1}H-NMR (400 MHz, CD_3OD) δ 8.60 (1H, d, $J = 2.2$ Hz), 8.16 (1H, dd, $J = 2.2$, 8.3 Hz), 7.48 (2H, d, $J = 9.0$ Hz), 7.44 (1H, d, $J = 8.3$ Hz), 7.29 (2H, d, $J = 2.2$ Hz), 7.14 (2H, dd, $J = 2.2$, 9.0 Hz), 4.29 (2H, s).

1-(4-Amidomethyl-fluorescein)-1,4,7,10-tetraazacyclododecane (4AMF-cyclen). A dry DMF suspension (10 mL) of 1,4,7,10-tetraazacyclododecane tetrahydrochloride (cyclen 4HCl) (318 mg, 1.0 mmol), K_2CO_3 (1.4 g, 10.1 mmol) and KI (1.7 g, 10.1 mmol) was stirred for 5 min at 80°C under anaerobic conditions. To the suspension was then slowly added 4AMF-Cl (424 mg, 1.0 mmol) in dry DMF solution (10 mL). After stirring for 9 h at 80°C, the suspension was filtered and the obtained residue was washed with MeCN. The residue was added to MeOH (20 mL). After stirring for 30 min, the reddish suspension was filtered and the obtained residue was washed with MeOH. The filtrate was concentrated by evaporation and the resulting residue was redissolved in a minimum amount of MeOH. The solution was poured into Et_2O (200 mL), and the resulting residue was washed with Et_2O by decantation three times. The powder was dried under vacuum to obtain 4AMF-cyclen (336 mg, 0.6 mmol, 60%) as a red powder. MS (ESI, pos.) m/z found 560 ($[M+H]^+$), calcd. 560. ^{1}H-NMR (400 MHz, DMSO-d_6) δ 8.38 (1H, s), 7.91 (1H, d, $J = 7.3$ Hz), 6.62 (3H, m), 6.52 (2H, s), 6.44 (2H, dd, $J = 1.9$, 8.7 Hz), 3.17 (2H, s), 2.66 (16H, br).

1-(4-Amidomethyl-fluorescein)-1,4,7,10-tetraazacyclododecane-4,7,10-triacetic acid (4AMF-DOTA). To MeOH solution containing 4AMF-cyclen (559.6 mg, 1.0 mmol) and Et_3N (1.4 mL, 10 mmol) was added $BrCH_2COOH$ (556 mg, 4.0 mmol) in MeOH (20 mL) solution at room temperature. The solution was then warmed to 60°C and stirred for 12 h. The mixture was evaporated to remove the solvent. The yellow residue was added to MeOH (20 mL). The suspension was centrifuged (1500 × g, 10 min) and the supernatant was removed. This procedure was repeated five times. The resulting powder was dried under vacuum to obtain 4AMF-DOTA (550.3 mg, 0.8 mmol, 75%) as a yellow powder. MS (ESI, neg.) m/z found 732 ($[M-H]^-$), calcd. 732.

^{1}H-NMR (400 MHz, DMSO-d_6) δ 8.24 (1H, s), 7.68 (1H, s), 6.50–6.70 (7H, m), 4.15 (6H, br), 3.16 (18H, m).

4AMF-DOTA(Nd). To 0.01 mol/L TEAAc buffer, pH 6.5, solution (2 mL) containing 4AMF-DOTA (7.3 mg, 10 μmol) was added $NdCl_3$ $6H_2O$ (4.3 mg, 15 μmol) in 0.01 mol/L TEAAc buffer, pH 6.5, solution (2 mL). After stirring for 1 h at room temperature, the resulting suspension was filtered. The filtrate was introduced into a preconditioned solid phase extraction column (Waters, stationary phase C_{18}) and the buffer and excess lanthanide ion were washed away with distilled water. The chelate was eluted using a 1:4 methanol:water mixture. The solvent was evaporated, and the residue was dried under vacuum to obtain 4AMF-DOTA(Nd) (5.4 mg, 6.2 μmol, 62%) as a yellow powder. MS(ESI, neg.) m/z found 882 ($[M-H]^-$), calcd. 882.

RESULTS AND DISCUSSION

Synthesis of 4AMF-DOTA(Nd)

4AMF-DOTA was synthesized from 4-aminofluorescein in three steps, as shown in Scheme 1. 4AMF-DOTA(Nd)

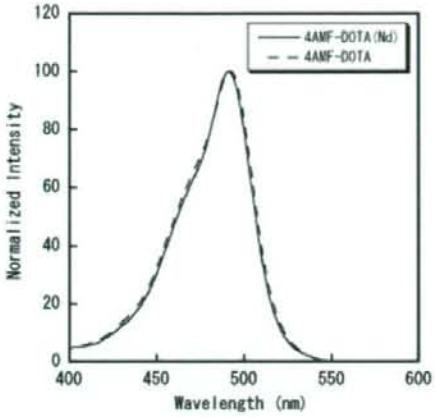

Figure 1. UV-vis absorption spectra of 4AMF-DOTA (dotted line) and 4AMF-DOTA(Nd) (solid line) in 10 mmol/L Tris–HCl buffer, pH 8.0.

was easily synthesized by stirring 4AMF-DOTA and $NdCl_3$ in TEAAc buffer, pH 6.5. Other lanthanide complexes, 4AMF-DOTA(Ln) (Ln = Eu, Tb and Yb), were prepared by the same method as for preparing 4AMF-DOTA(Nd), using $EuCl_3$, $TbCl_3$ and $YbCl_3$.

Spectroscopic characterizations of aqueous solution of 4AMF-DOTA(Nd)

UV-vis spectra of aqueous solutions of 4AMF-DOTA(Nd) and 4AMF-DOTA are shown in Fig. 1. These spectra showed the same features, suggesting that the chelation of DOTA to the Nd ion has no effect on the energy level of the fluorescein moiety.

With IR measurement, absorption of the carbonyl C=O stretching was observed at 1749 cm^{-1} for 4AMF-DOTA and 1724 cm^{-1} for 4AMF-DOTA(Nd), and absorption of the amide N–H bending was found at 1609 cm^{-1} for 4AMF-DOTA and 1587 cm^{-1} for 4AMF-DOTA(Nd) (data not shown). These shifts suggest that the three carbonyl groups and one amide group of the DOTA moiety participated in chelating the Nd ion.

The emission spectra of aqueous solutions of 4AMF-DOTA(Nd) and 4AMF-DOTA are shown in Fig. 2A. Although the long-wavelength tail of fluorescein fluorescence was observed in both compounds, two sharp peaks were detected at 870–900 nm in the spectrum of 4AMF-DOTA(Nd) compared with that of 4AMF-DOTA (Fig. 2A, λ_{ex} = 488 nm). These can be assigned to typical Nd $^4F_{3/2}$ to $^4I_{9/2}$ transition. This excitation wavelength is only slightly injurious to living cells. On the other hand, no fluorescent peak was detected for $NdCl_3$ and Nd-DOTA under the same conditions.

The excitation spectra of aqueous solutions of 4AMF-DOTA(Nd) and 4AMF-DOTA showed much the same features (Fig. 2B, λ_{em} = 870 nm for 4AMF-DOTA(Nd) and 515 nm for 4AMF-DOTA), thus supporting that the 870–900 nm luminescence shown in 4AMF-DOTA(Nd) is derived from the transfer of energy from an excited fluorescein moiety.

These results indicate that 4AMF-DOTA(Nd) can emit NIR fluorescence through its excitation by visible light as expected, but the fluorescence intensity is lower than that from fluorescein. This might occur partly because of the very low triplet yield of excited fluorescein. A simple model for the description of the sensitization process is shown in Fig. 3 (17). Energy transfer from fluorescein to the Nd ion occurs in the triplet state of fluorescein. Moreover, singlet energy transfer has been

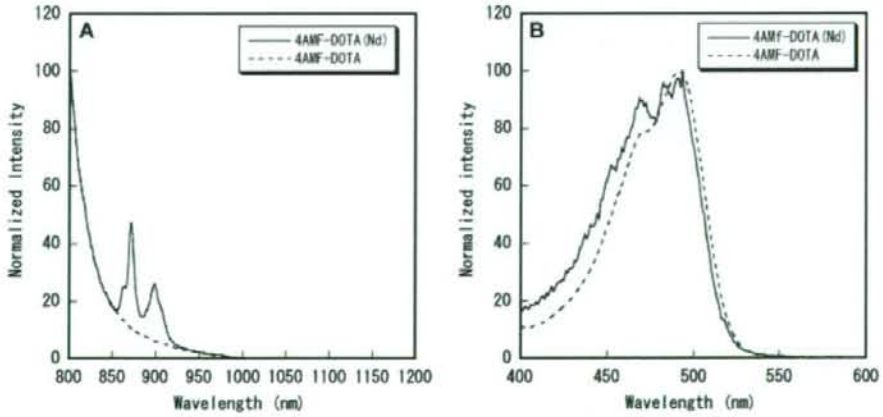

Figure 2. Spectroscopy of 4AMF-DOTA (dotted line) and 4AMF-DOTA(Nd) (solid line) in 10 mmol/L Tris–HCl buffer, pH 8.0. (A) Emission spectra (λ_{ex} = 488 nm). (B) Excitation spectra (λ_{ex} = 870 nm for 4AMF-DOTA(Nd) and 515 nm for 4AMF-DOTA).

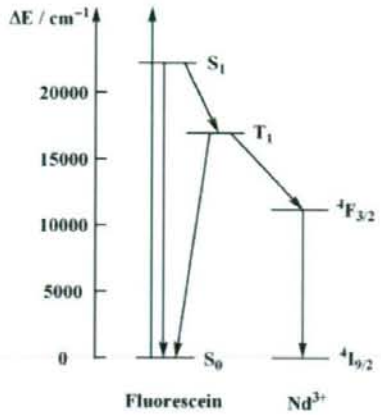

Figure 3. Simple photophysical scheme describing a possible pathway for sensitization of Nd luminescence in 4AMF-DOTA(Nd).

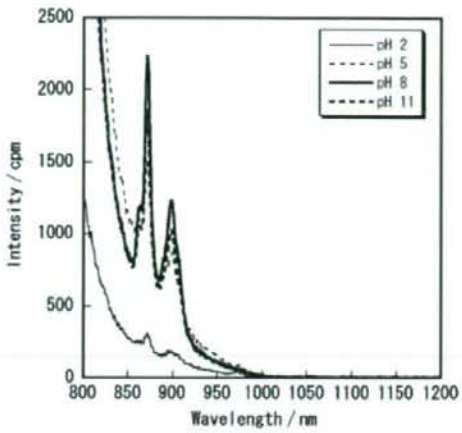

Figure 4. pH effect on the emission spectra of 4AMF-DOTA(Nd) in 10 mmol/L Britton–Robinson buffer.

shown not to contribute significantly to the sensitization process (18).

The energy transfer from the antenna to lanthanide ion has been studied previously (19–21), which has suggested several mechanisms, such as Förster energy transfer (19), Dexter exchange (20) and sequential electronic interaction (21), although none of them has been fully elucidated yet and the mechanism involved in 4AMF-DOTA(Nd) is also unclear. Refining the energy level of fluorescein through derivative syntheses (15) or the use of other chromophores (22, 23) suitable for the Nd ion can be an effective solution.

On the other hand, 4AMF-DOTA(Yb) showed a small peak at approximately 1000 nm due to typical ytterbium $^2F_{5/2}$ to $^2F_{7/2}$ transition, whereas emission peaks of 4AMF-DOTA(Eu) and 4AMF-DOTA(Tb) were not observed, owing to their high excitation levels.

Effects of pH and solvent on the fluorescence of 4AMF-DOTA(Nd)

The effect of pH on the fluorescence of 4AMF-DOTA(Nd) was examined (Fig. 4). The fluorescent intensity of 4AMF-DOTA(Nd) was weak at pH 2, increased with pH and peaked at pH 8. In the pH range 2–11, no degradation product was detected by electrospray mass spectral (ESI–MS) analysis, suggesting the high stability of 4AMF-DOTA(Nd).

It is well known that the fluorescence intensity emitted by fluorescein varies depending on the pH of solvents. The dianionic form of fluorescein in neutral and basic solutions is the most effective to emit fluorescence. In other words, in acidic solution, transition to the ground state of excited fluorescein is carried out without a fluorescent process (24). Therefore, the results shown in Fig. 4 should be regarded as a reflection of the characteristics of fluorescein, supporting the occurrence of energy transfer from fluorescein, the antenna moiety, to the Nd ion.

4AMF-DOTA(Nd) could easily dissolve in many polar organic solvents (e.g. MeOH, EtOH and DMSO). Figure 5 shows the emission spectra (Fig. 5A) and the excitation spectra (Fig. 5B) of 4AMF-DOTA(Nd) in 10 mmol/L Tris–HCl buffer, pH 8.0, and organic solvents such as MeOH, EtOH and DMSO. The λ_{max} of the excitation wavelength against 870 nm emission was 488 nm in aqueous buffer and 498, 504 and 523 nm in MeOH, EtOH and DMSO, respectively (Fig. 5B). On the other hand, the emission spectra showed the same features in the four tested solvents except for intensity at 870 nm and 890 nm (Fig. 5A). This difference in the wavelength shift between excitation and emission spectra may emphasize the orientation of fluorescence, i.e. the results can be considered as follows. In excitation spectra, changes of the λ_{max} in organic solvents are caused by the effect on the energy levels of fluorescein by the solvents, and in the emission spectra the constant wavelength in the four solvents is due to the characteristic of lanthanide ions, that 5s and 5d orbitals are located outside the 4f orbital responsible for fluorescence and protect it from environmental changes. In other words, these data further support that fluorescence around 870–900 nm derives from the Nd ion through energy transfer from the antenna moiety. The emission intensity of 4AMF-DOTA(Nd) shown more strongly in organic solvents than in buffer is probably because H_2O acts as a quencher against excited 4AMF-DOTA(Nd) in some processes.

Long-lived luminescence measurement

Time-resolved fluorescent (TRF) measurement can extract long-lived luminescence. Figure 6 shows the

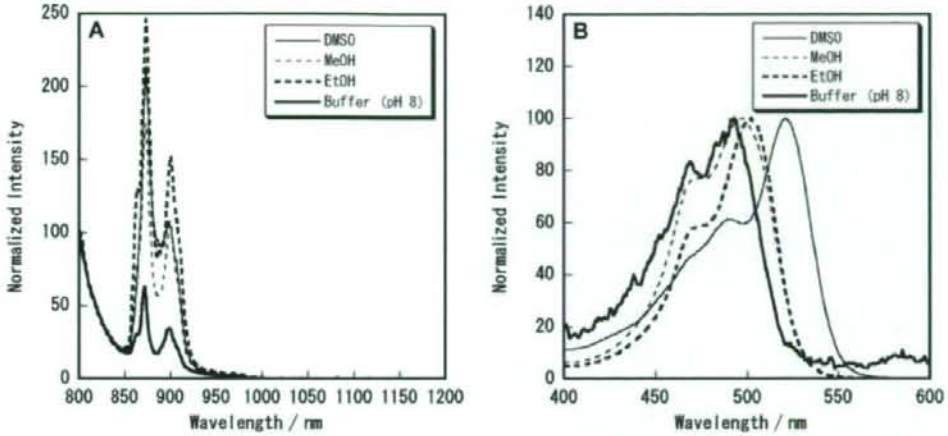

Figure 5. Solvent effect on (A) emission spectra and (B) excitation spectra of 4AMF-DOTA(Nd) in 10 mmol/L Tris–HCl buffer, pH 8.0, MeOH, EtOH and DMSO; each organic solvent contained 0.1% v/v Et_3N.

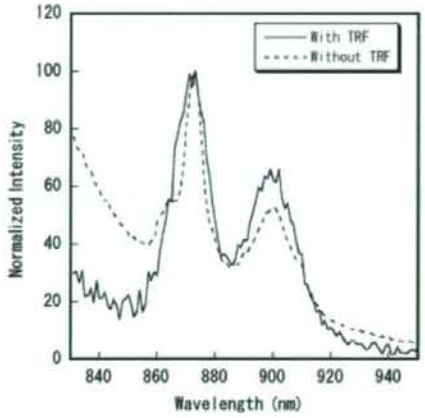

Figure 6. Emission spectra of 4AMF-DOTA(Nd) in 10 mmol/L Tris–HCl buffer, pH 8.0, with (solid line) and without (dotted line) time-resolved measurement.

emission spectra of 4AMF-DOTA(Nd) detected with (solid line) and without (dotted line) TRF measurement. The luminescence of fluorescein and the Nd ion was observed without TRF measurement, as also shown in Fig. 2A, whereas the luminescence of fluorescein disappeared in the detection of emission spectrum with TRF measurement, resulting in the extraction of only Nd luminescence. Furthermore, we calculated the lifetime of Nd ion luminescence using the equation described in the Experimental section. A lifetime of 2.3 μs was consequently obtained as reasonable for a Nd complex, as reported previously (10, 17). In view of the ns-order lifetime of fluorescein [~4 ns (25)], 4AMF-DOTA(Nd) can be considered a potential NIR fluorescent probe able to be detected and imaged separately from fluorescein, scattered or reflected excitation light and other organic fluorophores by the TRF technique.

CONCLUSION

The results obtained in this study indicate that 4AMF-DOTA(Nd) has the potential for *in vivo* fluorescence imaging, with several favourable properties, such as near-infrared luminescence, visible light excitation, long lifetime and large Stoke's shift.

Acknowledgement

This work was partly supported by the Twenty-first Century Center of Excellence Programme 'Knowledge Information Infrastructure for Genome Science'.

REFERENCES

1. Fu G, Yang HY, Wang C, Zhang F, You ZD, Wang GY, He C, Chen YZ, Xu ZZ. Detection of constitutive heterodimerization of the integrin Mac-1 subunits by fluorescence resonance energy transfer in living cells. *Biochem. Biophys. Res. Commun.* 2006; **346**: 986.
2. Wandelt B, Cywinski P, Darling GD, Stranix BR. Single cell measurement of micro-viscosity by ratio imaging of fluorescence of styrylpyridinium probe. *Biosens. Bioelectron.* 2005; **20**: 1728.
3. Mizukami S, Kikuchi K, Higuchi T, Urano Y, Mashima T, Tsuruo T, Nagano T. Imaging of caspase-3 activation in HeLa cells stimulated with etoposide using a novel fluorescent probe. *FEBS Lett.* 1999; **453**: 356.
4. Konig K. Multiphoton microscopy in life sciences. *J. Microsc.* 2000; **200**: 83.
5. Hansch A, Frey O, Sauner D, Hilger I, Haas M, Malich A, Brauer R, Kaiser WA. *In vivo* imaging of experimental arthritis with near-infrared fluorescence. *Arthrit. Rheum.* 2004; **50**: 961.

6. Chen X, Conti PS, Moats RA. *In vivo* near-infrared fluorescence imaging of integrin $\alpha v\beta 3$ in brain tumor xenografts. *Cancer Res.* 2004; **64**: 8009.
7. Wunder A, Tung CH, Muller-Ladner U, Weissleder R, Mahmood U. *In vivo* imaging of protease activity in arthritis: a novel approach for monitoring treatment response. *Arthrit. Rheum.* 2004; **50**: 2459.
8. Faulkner S, Carrie MC, Pope SJ, Squire J, Beeby A, Sammes PG. Pyrene-sensitized near-IR luminescence from ytterbium and neodymium complexes. *Dalton Trans.* 2004; 1405.
9. Beer PD, Szemes F, Passaniti P, Maestri M. Luminescent ruthenium(II) bipyridine-calix[4]arene complexes as receptors for lanthanide cations. *Inorg. Chem.* 2004; **43**: 3965.
10. Hasegawa Y, Ohkubo T, Sogabe K, Kawamura Y, Wada Y, Nakashima N, Yanagida S. Luminescence of novel neodymium sulfonylaminate complexes in organic media. *Angew. Chem. Int. Ed. Engl.* 2000; **39**: 357.
11. Becker CF, Clayton D, Shapovalov G, Lester HA, Kochendoerfer GG. On-resin assembly of a linkerless lanthanide(III)-based luminescence label and its application to the total synthesis of site-specifically labeled mechanosensitive channels. *Bioconjug. Chem.* 2004; **15**: 1118.
12. Wu SL, Horrocks WD. Direct determination of stability constants of lanthanide ion chelates by laser-excited europium(III) luminescence spectroscopy: application to cyclic and acyclic aminocarboxylate complexes. *J. Chem. Soc. Dalton* 1997; 1497.
13. Quici S, Marzanni G, Forni A, Accorsi G, Barigelletti F. New lanthanide complexes for sensitized visible and near-IR light emission: synthesis, ^{1}H-NMR, and X-ray structural investigation and photophysical properties. *Inorg. Chem.* 2004; **43**: 1294.
14. Werts MHV, Hofstraat JW, Geurts FAJ, Verhoeven JW. Fluorescein and eosin as sensitizing chromophores in near-infrared luminescent ytterbium(III), neodymium(III) and erbium(III) chelates. *Chem. Phys. Lett.* 1997; **276**: 196.
15. Nolan EM, Burdette SC, Harvey JH, Hilderbrand SA, Lippard SJ. Synthesis and characterization of zinc sensors based on a monosubstituted fluorescein platform. *Inorg. Chem.* 2004; **43**: 2624.
16. Brown L, Halling PJ, Johnston GA, Suckling CJ, Valivety RH. The synthesis of some water-insoluble dyes for the measurement of pH in water-immiscible solvents. *J. Chem. Soc. Perk. Trans.* **1**: 1990; 3349.
17. Bassett AP, Magennis SW, Glover PB, Lewis DJ, Spencer N, Parsons S, Williams RM, De Cola L, Pikramenou Z. Highly luminescent, triple- and quadruple-stranded, dinuclear Eu, Nd, and Sm(III) lanthanide complexes based on bis-diketonate ligands. *J. Am. Chem. Soc.* 2004; **126**: 9413.
18. Crosby GA, Alire RM, Whan RE. Intramolecular energy transfer in rare earth chelates – role of triplet state. *J. Chem. Phys.* 1961; **34**: 743.
19. Clarkson IM, Beeby A, Bruce JI, Govenlock LJ, Lowe MP, Mathieu CE, Parker D, Senanayake K. Experimental assessment of the efficacy of sensitized emission in water from a europium ion, following intramolecular excitation by a phenanthridinyl group. *N. J. Chem.* 2000; **24**: 377.
20. Barigelletti F, Flamigni L, Balzani V, Collin JP, Sauvage JP, Sour A, Constable EC, Thompson AMWC. Intramolecular energy transfer through phenyl bridges in rod-like dinuclear Ru(II)/Os(II) terpyridine-type complexes. *Coord. Chem. Rev.* 1994; **132**: 209.
21. Faulkner S, Burton-Pye BP, Khan T, Martin LR, Wray SD, Skabara PJ. Interaction between tetrathiafulvalene carboxylic acid and ytterbium D03A: solution state self-assembly of a ternary complex which is luminescent in the near IR. *Chem. Commun.* 2002; 1668.
22. Gunnlaugsson T, MacDonaill DA, Parker D. Lanthanide macrocyclic quinolyl conjugates as luminescent molecular-level devices. *J. Am. Chem. Soc.* 2001; **123**: 12866.
23. Quici S, Marzanni G, Cavazzini M, Anelli PL, Botta M, Gianolio E, Accorsi G, Armaroli N, Barigelletti F. Highly luminescent Eu^{3+} and Tb^{3+} macrocyclic complexes bearing an appended phenanthroline chromophore. *Inorg. Chem.* 2002; **41**: 2777.
24. Urano Y, Kamiya M, Kanda K, Ueno T, Hirose K, Nagano T. Evolution of fluorescein as a platform for finely tunable fluorescence probes. *J. Am. Chem. Soc.* 2005; **127**: 4888.
25. Thevenin BJM, Periasamy N, Shohet SB, Verkman AS. Segmental dynamics of the cytoplasmic domain of erythrocyte band 3 determined by time-resolved fluorescence anisotropy – sensitivity to pH and ligand-binding. *Proc. Natl Acad. Sci. USA* 1994; **91**: 1741.

Bioorganic & Medicinal Chemistry xxx (2009) xxx–xxx

Contents lists available at ScienceDirect

Bioorganic & Medicinal Chemistry

journal homepage: www.elsevier.com/locate/bmc

^{18}F-labeled flavones for in vivo imaging of β-amyloid plaques in Alzheimer's brains

Masahiro Ono [a,b,*], Rumi Watanabe [a], Hidekazu Kawashima [c], Tomoki Kawai [b], Hiroyuki Watanabe [a], Mamoru Haratake [a], Hideo Saji [b], Morio Nakayama [a,*]

[a] Graduate School of Biomedical Sciences, Nagasaki University, 1-14 Bunkyo-machi, Nagasaki 852-8521, Japan
[b] Graduate School of Pharmaceutical Sciences, Kyoto University, 46-29 Yoshida Shimoadachi-cho, Sakyo-ku, Kyoto 606-8501, Japan
[c] Graduate School of Medicine, Kyoto University, Shogoin Kawahara-cho, Sakyo-ku, Kyoto 606-8507, Japan

ARTICLE INFO

Article history:
Received 10 December 2008
Revised 6 January 2009
Accepted 7 January 2009
Available online xxxx

Keywords:
Alzheimer's disease
β-Amyloid plaque
PET
Flavone

ABSTRACT

In vivo imaging of β-amyloid (Aβ) aggregates in the brain may lead to early detection of Alzheimer's disease (AD) and monitoring of the progression and effectiveness of treatment. The purpose of this study was to develop novel ^{18}F-labeled amyloid-imaging probes based on flavones as a core structure. Fluoropegylated (FPEG) flavone derivatives were designed and synthesized. The affinity of the derivatives for Aβ aggregates varied from 5 to 321 nM. In brain sections of AD model mice, FPEG flavones with the dimethylamino group intensely stained β-amyloid plaques. In biodistrubution experiments using normal mice, they displayed high uptake in the brain ranging from 2.9 to 4.2%ID/g at 2 min postinjection. The radioactivity washed out from the brain rapidly (1.3–2.0%ID/g at 30 min), which is highly desirable for β-amyloid imaging agents. FPEG flavones may be potential PET imaging agents for β-amyloid plaques in Alzheimer's brains.

1. Introduction

Alzheimer's disease (AD) is a progressive neurodegenerative disorder characterized by cognitive decline, irreversible memory loss, disorientation, and language impairment. The presence of β-amyloid (Aβ) aggregates in the brain is generally accepted as a hallmark of AD.[1,2] Since the only definitive diagnosis of AD is by pathological examination of postmortem staining of affected brain tissues, the development of techniques which enable one to image β-amyloid plaques in vivo has been strongly desired.[3–5]

Recent success in developing radiolabeled agents targeting Aβ aggregates has provided a window of opportunity to improve the diagnosis of AD. Preliminary reports of positron emission tomography (PET) imaging suggested that [^{11}C]4-*N*-methylamino-4′-hydroxystilbene (SB-13),[6,7] [^{11}C] 2-(4′-(methylaminophenyl)-6-hydroxy benzothiazole (PIB),[8,9] and [^{11}C]2-(2-[2-dimethylaminothiazol-5-yl]ethenyl)-6-(2-[fluoro]ethoxy)benzoxazole (BF-227)[10] showed differential uptake and retention in the brain of AD patients as compared to controls. But ^{11}C is a positron-emitting isotope with a short $t_{1/2}$ (20 min), which limits its clinical application. Recent efforts have focused on the development of comparable agents labeled with a longer half-life isotope, ^{18}F ($t_{1/2}$: 110 min). Preliminary studies with [^{18}F]-2-(1-(2-(*N*-(2-fluoroethyl)-*N*-methylamino)-naphthalen-6-yl)ethylidene)malononitrile ([^{18}F]FDDNP)[11,12] showed differential uptake and retention in the brain of AD patients for the first time. More recently, a stilbene derivative, [^{18}F]BAY94-9172, has been shown to be useful for the imaging of β-amyloid plaques in living human brain tissue in clinical trials.[13]

To search for more candidates for ^{18}F-labeled β-amyloid imaging agents for PET, we planned to evaluate a new series of flavone derivatives previously reported as useful for imaging β-amyloid by single photon emission computed tomography (SPECT).[14] The derivatives showed good affinity for Aβ aggregates in vitro in binding experiments using synthetic Aβ aggregates and neuropathological staining of AD brain sections, suggesting these classes of radioiodinated flavones to be potential imaging agents.

Recently, Kung et al. exploited a novel approach by using fluoro-pegylation (FPEG) of the core structure for ^{18}F labeling of derivatives.[15] Since this approach offers a simple and easy way to incorporate ^{18}F into the target without an appreciable increase in lipophilicity, we planned to apply it to the labeling of flavone derivatives. In addition to the structural characteristics of flavone as the pharmacophore, it has been shown that electron-donating groups such as amino, methylamino, dimethylamino, methoxy, or hydroxy groups play a critical role in the binding of Aβ aggregates.[6,8,16,17] With these considerations, we designed 12 fluorinated flavones with a fluorine or FPEGylation at position 4 and an electron-donating group at position 4′ (Fig. 1).

* Corresponding authors. Tel.: +81 75 753 4608; fax: +81 75 753 4568 (M.O.); tel./fax: +81 95 819 2441 (M.N.).
E-mail addresses: ono@pharm.kyoto-u.ac.jp, mono@net.nagasaki-u.ac.jp (M. Ono) morio@nagasaki-u.ac.jp (M. Nakayama).

0968-0896/$ - see front matter © 2009 Elsevier Ltd. All rights reserved.
doi:10.1016/j.bmc.2009.01.025

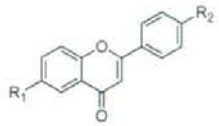

Compound	R_1	R_2
8a	FCH_2CH_2O	$N(CH_3)_2$
8b	$F(CH_2CH_2O)_2$	$N(CH_3)_2$
8c	$F(CH_2CH_2O)_3$	$N(CH_3)_2$
12	FCH_2CH_2O	NH_2
13	FCH_2CH_2O	$NHCH_3$
15b	$F(CH_2CH_2O)_2$	NH_2
15c	$F(CH_2CH_2O)_3$	NH_2
17b	$F(CH_2CH_2O)_2$	$NHCH_3$
17c	$F(CH_2CH_2O)_3$	$NHCH_3$
21	F	NH_2
22	F	$NHCH_3$
23	F	$N(CH_3)_2$

Figure 1. Chemical structure of FPEG-flavone derivatives.

We report here the in vitro and in vivo evaluation of a new series of flavone derivatives as agents for imaging β-amyloid with PET.

2. Experimental

All reagents were commercial products and used without further purification unless otherwise indicated. ^{1}H NMR spectra were obtained on a Varian Gemini 300 spectrometer with TMS as an internal standard. Coupling constants are reported in hertz. Multiplicity is defined by s (singlet), d (doublet), t (triplet), br (broad), and m (multiplet). Mass spectra were obtained on a JEOL IMS-DX instrument.

2.1. Chemistry

2.1.1. 4-Nitrobenzoic acid 2-acetyl-4-methoxyphenyl ester (1)

To a stirring solution of 4-nitrobenzoyl chloride (1.8 g, 10 mmol) in pyridine (20 mL) was added 2-hydroxy-5-methoxyacetophenone (1.6 g, 10 mmol). The reaction mixture was stirred at room temperature for 3 h, and poured into a 1 N aqueous HCl/ice solution with vigorous stirring. The precipitate that formed was filtered and washed with water to yield acetophenone **1** (2.9 g, 90.4% yield). ^{1}H NMR (300 MHz, $CDCl_3$) δ: 2.54 (s, 3H), 3.89 (s, 3H), 7.15–7.16 (m, 2H), 7.38 (d, J = 2.0 Hz, 1H), 8.37 (s, 4H).

2.1.2. 1-(5-Methoxy-2-hydroxyphenyl)-3-(4-nitrophenyl)propane-1,3-dione (2)

A solution of acetophenone **1** (2.9 g, 9.0 mmol) and pyridine (50 mL) was heated to 50 °C, and to it was added pulverized potassium hydroxide (2.5 g, 45.2 mmol). The reaction mixture was stirred for 90 min, and when it had cooled, 30 mL of 10% aqueous acetic acid solution was added. The yellow precipitate that formed was filtered to yield **2** (2.5 g, 88.1% yield). ^{1}H NMR (300 MHz, $CDCl_3$) δ: 3.85 (s, 3H), 6.84 (s, 1H), 6.99 (d, J = 6.9 Hz, 1H), 7.15–7.18 (m, 1H), 7.22 (d, J = 2.2 Hz, 1H), 8.10 (d, J = 6.6 Hz, 2H), 8.35 (d, J = 6.6 Hz, 2H), 11.5 (s, 1H).

2.1.3. 6-Methoxy-4′-nitroflavone (3)

A mixture of the diketone **2** (2.5 g, 8.0 mmol), concentrated sulfuric acid (2 mL), and glacial acetic acid (40 mL) was heated at 100 °C for 2 h and cooled to room temperature. The mixture was poured onto crushed ice, and the resulting precipitate was filtered to yield **3** (1.5 g, 63.5%). ^{1}H NMR (300 MHz, $CDCl_3$) δ: 3.93 (s, 3H), 6.92 (s, 1H), 7.31–7.37 (m, 1H), 7.54–7.61 (m, 2H), 8.11 (d, J = 9.3 Hz, 2H), 8.39 (d, J = 9.3 Hz, 2H).

2.1.4. 6-Methoxy-4′-aminoflavone (4)

A mixture of **3** (3.0 g, 10.2 mmol), $SnCl_2$ (7.6 g, 39.8 mmol), and EtOH (30 mL) was stirred under reflux for 40 min. After the mixture had cooled to room temperature, 1 M NaOH (50 mL) was added until the mixture became alkaline. After extraction with ethyl acetate, the combined organic layers were washed with brine, dried over Na_2SO_4, and filtered. The solvent was removed, and the residue was purified by silica gel chromatography (hexane/ethyl acetate = 1:2) to give 1.3 g of **4** (65.3% yield). ^{1}H NMR (300 MHz, $CDCl_3$) δ: 3.91 (s, 3H), 4.11 (s, broad, 2H), 6.69 (s, 1H), 6.75 (d, J = 6.6 Hz, 2H), 7.24–7.27 (m, 1H), 7.47 (d, J = 6.6 Hz, 1H), 7.59 (d, J = 2.2 Hz, 1H), 7.75 (d, J = 6.6 Hz, 2H).

2.1.5. 6-Methoxy-4′-dimethylaminoflavone (5)

To a mixture of **4** (401 mg, 1.5 mmol) and paraformaldehyde (450 mg, 15 mmol) in AcOH (10 mL) was added $NaCNBH_3$ (471 mg, 7.5 mmol) in one portion at room temperature. The resulting mixture was stirred at room temperature for 1.5 h, and the addition of 1 M NaOH was followed by extraction with CH_3Cl. The organic phase was dried over Na_2SO_4. The solvent was removed, and the residue was purified by silica gel chromatography ($CHCl_3$/MeOH = 20:1) to give 371 mg of **5** (83.7% yield). ^{1}H NMR (300 MHz, $CDCl_3$) δ: 3.07 (s, 6H), 3.91 (s, 3H), 6.70 (s, 1H), 6.75 (d, J = 9.0 Hz, 2H), 7.24–7.26 (m, 1H), 7.47 (d, J = 9.0 Hz, 1H), 7.59 (d, J = 2.2 Hz, 1H), 7.81 (d, J = 9.0 Hz, 2H).

2.1.6. 6-Hydroxy-4′-dimethylaminoflavone (6)

To a solution of **5** (371 mg, 1.5 mmol) in CH_2Cl_2 (10 mL) at 10 °C was added BBr_3 (7.5 mL, 1 M solution in CH_2Cl_2) dropwise in an ice bath. The mixture was allowed to warm to room temperature and was stirred for 12 h. Water was added while the reaction mixture was cooled in an ice bath to keep the reaction temperature at 0 °C. After extraction with CH_2Cl_2, the combined organic phase was dried over Na_2SO_4. The filtrate was concentrated and the residue was purified by silica gel chromatography ($CHCl_3$/MeOH = 20:1) to give 303 mg of **6** (71.8% yield). ^{1}H NMR (300 MHz, $CDCl_3$) δ: 3.05 (s, 6H), 6.74 (d, J = 9.3 Hz, 2H), 7.26 (d, J = 3.0 Hz, 1H), 7.45 (d, J = 9.0 Hz, 1H), 7.58 (d, J = 3.0 Hz, 1H), 7.77 (d, J = 9.0 Hz, 2H).

2.1.7. 6-Hydroxyethoxy-4′-dimethylaminoflavone (7a)

To a solution of **6** (85 mg, 0.30 mmol) and ethylene chlorohydrin (100 μL, 1.50 mmol) in DMSO (3 mL) was added anhydrous K_2CO_3 (41 mg, 0.90 mmol). The reaction mixture was stirred at 120 °C for 48 h, then poured into water. After extraction with chloroform, the organic layers were combined and dried over Na_2SO_4. Evaporation of the solvent afforded a residue, which was purified by silica gel chromatography ($CHCl_3$/MeOH = 33:1) to give 30 mg of **7a** (30.5%). ^{1}H NMR (300 MHz, $CDCl_3$) δ: 3.06 (s, 6H), 3.98–4.05 (m, 2H), 4.17–4.23 (m, 2H), 6.69 (s, 1H), 6.76 (d, J = 9.3 Hz, 2H), 7.28 (d, J = 3.0 Hz, 1H), 7.47 (d, J = 9.0 Hz, 1H), 7.60 (d, J = 3.0 Hz, 1H), 7.80 (d, J = 9.0 Hz, 2H).

2.1.8. 6-(2-(2-Hydroxy-ethoxy)-ethoxy)-4′-dimethylaminoflavone (7b)

To a solution of **6** (82 mg, 0.29 mmol) and ethylene glycol mono-2-chloroethyl ether (37 μL, 0.35 mmol) in DMF (3 mL) was added anhydrous K_2CO_3 (120 mg, 0.87 mmol). The reaction mixture was stirred at 120 °C for 11 h, then poured into water. After extraction with chloroform, the organic layers were combined and dried over Na_2SO_4. Evaporation of the solvent afforded a residue, which was purified by silica gel chromatography (hexane/ethyl acetate = 10:1) to give 107 mg of **7b** (99.3%). ^{1}H NMR (300 MHz, $CDCl_3$) δ: 3.07 (s, 6H), 3.69 (t, J = 5.1 Hz, 2H), 3.79 (s, 2H), 3.91 (t, J = 4.5 Hz, 2H), 4.26 (t, J = 4.5 Hz, 2H), 6.69 (s, 1H), 6.75 (d, J = 9.0 Hz, 2H), 7.27–7.30 (m, 1H), 7.47 (d, J = 9.0 Hz, 1H), 7.64 (d, J = 2.2, 1H), 7.81 (d, J = 9.0 Hz, 2H).

Please cite this article in press as: Ono, M. et al., *Bioorg. Med. Chem.* (2009), doi:10.1016/j.bmc.2009.01.025

2.1.9. 6-(2-(2-(2-Hydroxy-ethoxy)-ethoxy)ethoxy)-4′-dimethylaminoflavone (7c)

To a solution of **6** (100 mg, 0.36 mmol) and 2-[2-(2-chloroethoxy)ethoxy]ethanol (62 μL, 0.43 mmol) in DMF (3 mL) was added anhydrous K_2CO_3 (148 mg, 1.07 mmol). The reaction mixture was stirred at 120 °C for 17 h, then poured into water. After extraction with chloroform, the organic layers were combined and dried over Na_2SO_4. Evaporation of the solvent afforded a residue, which was purified by preparative TLC ($CHCl_3$/MeOH = 20:1) to give 76 mg of **7c** (51.1%). ^1H NMR (300 MHz, $CDCl_3$) δ: 3.07 (s, 6H), 3.62–3.76 (m, 8H), 3.91 (t, J = 4.5 Hz, 2H), 4.26 (t, J = 4.5 Hz, 2H), 6.69 (s, 1H), 6.77 (d, J = 9.3 Hz, 2H), 7.28–7.33 (m, 1H), 7.47 (d, J = 9.0 Hz, 1H), 7.60 (d, J = 2.2, 1H), 7.81 (d, J = 9.0 Hz, 2H).

2.1.10. 6-Fluoroethoxy-4′-dimethylaminoflavone (8a)

To a solution of **7a** (30 mg, 0.09 mmol) in ethylene glycol dimethyl ether (3 mL) was added dimethylamino sulfur trifluoride (DAST) (30 μL, 0.23 mmol) in a dry ice-acetone bath. The reaction mixture was stirred for 6 h at room temperature. The mixture was then poured into a saturated $NaHSO_3$ solution and after extraction with chloroform, the organic phase was separated, dried over Na_2SO_4, and filtered. The residue was purified by silica gel chromatography (hexane/ethyl acetate = 2:1) to give 16 mg of **8a** (53.0%). ^1H NMR (300 MHz, $CDCl_3$) δ: 2.93 (s, 6H), 4.26–4.40 (m, 2H), 4.70–4.92 (m, 2H), 6.71 (s, 1H), 6.76 (d, J = 9.0 Hz, 2H), 7.29–7.35 (m, 1H), 7.50 (d, J = 9.0 Hz, 1H), 7.59 (d, J = 3.3 Hz, 1H), 7.82 (d, J = 9.3 Hz, 2H). EI-MS m/z 327 (M^+).

2.1.11. 6-(2-(2-Fluoro-ethoxy)-ethoxy)-4′-dimethylaminoflavone (8b)

To a solution of **7b** (29 mg, 0.08 mmol) in 1,2-dimethoxyethane (DME) (5 mL) was added DAST (21 μL, 0.16 mmol) in a dry ice-acetone bath. The reaction mixture was stirred for 1.5 h at room temperature. The mixture was then poured into a saturated $NaHSO_3$ solution and after extraction with chloroform, after the organic phase was separated, dried over Na_2SO_4, and filtered. The residue was purified by preparative TLC ($CHCl_3$/MeOH = 20:1) to give 15 mg of **8b** (51.5%). ^1H NMR (300 MHz, $CDCl_3$) δ: 3.07 (s, 6H), 3.79 (t, J = 4.2 Hz, 1H), 3.89–3.96 (m, 3H), 4.26 (t, J = 4.8 Hz, 2H), 4.54 (t, J = 4.2 Hz), 4.69 (t, J = 4.2 Hz), 6.70 (s, 1H), 6.76 (d, J = 9.0 Hz, 2H), 7.27–7.33 (m, 1H), 7.49 (d, J = 9.3 Hz, 1H), 7.59 (d, J = 3.0, 1H), 7.81 (d, J = 9.0 Hz, 2H). EI-MS m/z 371 (M^+).

2.1.12. 6-(2-(2-(2-Fluoro-ethoxy)-ethoxy)ethoxy)-4′-dimethylaminoflavone (8c)

To a solution of **7c** (141 mg, 0.34 mmol) in DME (5 mL) was added DAST (90 μL, 0.68 mmol) in a dry ice-acetone bath. The reaction mixture was stirred for 1 h at room temperature. The mixture was then poured into saturated $NaHSO_3$ solution and extracted with chloroform. After the organic phase was separated, dried over Na_2SO_4 and filtered, the residue was purified by preparative TLC (hexane/ethyl acetate = 1:5) to give 21 mg of **8c** (14.9%). ^1H NMR ($CDCl_3$) δ: 3.08 (s, 6H), 3.69–3.81 (m, 6H), 3.91 (t, J = 4.8 Hz, 2H), 4.24 (t, J = 4.8 Hz, 2H), 4.49 (t, J = 4.5 Hz, 1H), 4.65 (t, J = 4.5 Hz, 1H), 6.69 (s, 1H), 6.76 (d, J = 9.0 Hz, 2H), 7.27–7.33 (m, 1H), 7.48 (d, J = 9.0 Hz, 1H), 7.59 (d, J = 2.2, 1H), 7.81 (d, J = 9.0 Hz, 2H). EI-MS m/z 415 (M^+).

2.1.13. 6-Hydroxy-4′-nitroflavone (9)

The same reaction as described above to prepare **6** was used, and 560 mg of **9** was obtained from **3** and BBr_3. EI-MS m/z 283 (M^+).

2.1.14. 6-(2-Hydroxy-ethoxy)-4′-nitroflavone (10a)

The same reaction as described above to prepare **7a** was used, and 40 mg of **10a** was obtained from **9** in a yield of 9.9%. ^1H NMR (300 MHz, $CDCl_3$) δ: 3.88–4.02 (m, 2H), 4.13–4.20 (m, 2H), 6.89 (s, 1H), 7.38–7.41 (m, 1H), 7.59 (d, J = 9.3 Hz, 1H), 7.67 (d, J = 3.3 Hz, 1H), 8.12 (d, J = 9.0 Hz, 2H), 8.46 (d, J = 9.0 Hz, 2H).

2.1.15. 6-(2-(2-Hydroxy-ethoxy)-ethoxy)-4′-nitroflavone (10b)

The same reaction as described above to prepare **7b** was used, and 830 mg of **10b** was obtained from **9**. ^1H NMR (300 MHz, $CDCl_3$) δ: 3.70 (t, J = 5.1 Hz, 2H), 3.79 (s, 2H), 3.93 (t, J = 5.0 Hz, 2H), 4.28 (t, J = 4.8 Hz, 2H), 6.90 (s, 1H), 7.37–7.41 (m, 1H), 7.56 (d, J = 9.3 Hz, 1H), 7.66 (d, J = 3.3 Hz, 1H), 8.10 (d, J = 9.0 Hz, 2H), 8.40 (d, J = 9.0 Hz, 2H).

2.1.16. 6-(2-(2-(2-Hydroxy-ethoxy)-ethoxy)ethoxy)-4′-nitroflavone (10c)

The same reaction as described above to prepare **7c** was used, and **10c** was obtained from **9** in a yield of 83.1%. ^1H NMR (300 MHz, $CDCl_3$) δ: 3.64 (t, J = 4.5 Hz, 2H), 3.71–3.78 (m, 6H), 3.93 (t, J = 4.8 Hz, 2H), 4.27 (t, J = 4.5 Hz, 2H), 6.90 (s, 1H), 7.38–7.42 (m, 1H), 7.55 (d, J = 9.0 Hz, 1H), 7.61 (d, J = 3.1 Hz, 1H), 8.10 (d, J = 8.7 Hz, 2H), 8.39 (d, J = 8.7 Hz, 2H). EI-MS m/z 415 (M^+).

2.1.17. 6-(2-Fluoro-ethoxy)-4′-nitroflavone (11)

The same reaction as described above to prepare **8a** was used, and 24 mg of **11** was obtained from **10a** in a yield of 41.6%. ^1H NMR (300 MHz, $CDCl_3$) 4.26–4.41 (m, 2H), 4.71–4.92 (m, 2H), 6.91 (s, 1H), 7.42–7.44 (m, 1H), 7.56–7.61 (m, 2H), 8.11 (d, J = 9.0 Hz, 2H), 8.39 (d, J = 9.3 Hz, 2H).

2.1.18. 6-(2-Fluoro-ethoxy)-4′-aminoflavone (12)

The same reaction as described above to prepare **4** was used, and 22 mg of **12** was obtained from **11** in a yield of 41.6%. ^1H NMR (300 MHz, $CDCl_3$) 4.10 (s, 2H), 4.27–4.39 (m, 2H), 4.71–4.88 (m, 2H), 6.70 (s, 1H), 6.76 (d, J = 9.0 Hz, 2H), 7.29–7.35 (m, 1H), 7.49 (d, J = 9.3 Hz, 1H), 7.58 (s, 1H), 7.75 (d, J = 9.0 Hz, 2H). EI-MS m/z 299 (M^+).

2.1.19. 6-(2-Fluoro-ethoxy)-4′-methylaminoflavone (13)

To a solution of **12** (22 mg, 0.07 mmol) in DMSO (2 mL) were added methyl iodide (0.14 mL) and K_2CO_3 (50.8 mg, 0.37 mmol). The reaction mixture was stirred at room temperature for 5 h, and poured into water (30 mL). After extraction with ethyl acetate (2 × 30 mL), the organic layers were combined and dried over Na_2SO_4. Evaporation of the solvent afforded a residue, which was purified by reversed phase HPLC (acetonitrile/H_2O = 3:2) to give 10 mg of **13** (43.4% yield). ^1H NMR (300 MHz, $CDCl_3$) 2.93 (s, 3H), 4.22 (s, 1H), 4.26–4.40 (m, 2H), 4.70–4.91 (m, 2H), 6.71 (s, 1H), 6.76 (d, J = 9.0 Hz, 2H), 7.29–7.35 (m, 1H), 7.50 (d, J = 9.3 Hz, 1H), 7.58 (s, 1H), 7.78 (d, J = 8.7 Hz, 2H). EI-MS m/z 313 (M^+).

2.1.20. 6-(2-(2-Hydroxy-ethoxy)-ethoxy)-4′-aminoflavone (14b)

The same reaction as described above to prepare **4** was used, and 251 mg of **14b** was obtained from **10b** in a yield of 37.9%. ^1H NMR ($CDCl_3$) δ: 3.69 (t, J = 5.1 Hz, 2H), 3.79 (s, 2H), 3.91 (t, J = 4.5 Hz, 2H), 4.09 (s, 2H), 4.27 (t, J = 4.2 Hz, 2H), 6.69 (s, 1H), 6.76 (d, J = 8.7 Hz, 2H), 7.27–7.32 (m, 1H), 7.48 (d, J = 9.3 Hz, 1H), 7.65 (d, J = 3.0 Hz, 1H), 7.75 (d, J = 8.4 Hz, 2H). EI-MS m/z 387 (M^+).

2.1.21. 6-(2-(2-(2-Hydroxy-ethoxy)-ethoxy)ethoxy)-4′-aminoflavone (14c)

The same reaction as described above to prepare **4** was used, and 553 mg of **14c** was obtained from **10c** in a yield of 58.8%. ^1H NMR (300 MHz, $CDCl_3$) δ: 3.62–3.65 (m, 2H), 3.71–3.78 (m, 6H), 3.91 (t, J = 4.8 Hz, 2H), 4.11 (s, 2H), 4.25 (t, J = 4.5 Hz, 2H), 6.68 (s, 1H), 6.75 (d, J = 8.7 Hz, 2H), 7.27–7.32 (m, 1H), 7.50 (d, J = 9.0 Hz, 1H), 7.59 (d, J = 2.2 Hz, 1H), 7.74 (d, J = 8.7 Hz, 2H). EI-MS m/z 387 (M^+).

Please cite this article in press as: Ono, M. et al., *Bioorg. Med. Chem.* (2009), doi:10.1016/j.bmc.2009.01.025

2.1.22. 6-(2-(2-Fluoro-ethoxy)-ethoxy)-4′-aminoflavone (15b)

The same reaction as described above to prepare **8b** was used, and 10 mg of **15b** was obtained from **14b** in a yield of 9.1%. ^{1}H NMR ($CDCl_3$) δ: 3.79 (t, J = 4.2 Hz, 1H), 3.86–3.95 (m, 3H), 4.11 (s, 2H), 4.25 (t, J = 4.5 Hz, 2H), 4.53 (t, J = 4.2 Hz, 1H), 4.70 (t, J = 4.2 Hz, 1H), 6.68 (s, 1H), 6.75 (d, J = 9.0 Hz, 2H), 7.28–7.33 (m, 1H), 7.47 (d, J = 9.0 Hz, 1H), 7.58 (d, J = 3.0 Hz, 1H), 7.74 (d, J = 8.4 Hz, 2H). EI-MS m/z 343 (M^+).

2.1.23. 6-(2-(2-(2-Fluoro-ethoxy)-ethoxy)ethoxy)-4′-aminoflavone (15c)

The same reaction as described above to prepare **8** was used, and 85 mg of **15c** was obtained from **14** in a yield of 81.3%. ^{1}H NMR ($CDCl_3$) δ: 3.62–3.65 (m, 2H), 3.70–3.78 (m, 7H), 3.82 (t, J = 3.9 Hz, 1H), 3.90 (t, J = 4.5 Hz, 2H), 4.22 (t, J = 4.5 Hz, 2H), 4.49 (t, J = 4.2 Hz, 1H), 4.66 (t, J = 4.2 Hz, 1H), 6.68 (s, 1H), 6.75 (d, J = 8.7 Hz, 2H), 7.27–7.32 (m, 1H), 7.46 (d, J = 9.3 Hz, 1H), 7.57 (d, J = 2.2 Hz, 1H), 7.73 (d, J = 8.7 Hz, 2H).

2.1.24. 6-(2-(2-Hydroxy-ethoxy)-ethoxy)-4′-methylaminoflavone (16b)

The same reaction as described above to prepare **13** was used, and 41 mg of **16b** was obtained from **14b** in a yield of 37.9%. ^{1}H NMR ($CDCl_3$) δ: 3.49 (s, 3H), 3.69 (t, J = 3.6 Hz, 2H), 3.77–3.79 (m, 2H), 3.91 (t, J = 4.8 Hz, 2H), 4.27 (t, J = 4.0 Hz, 2H), 6.65 (s, 1H), 6.68–6.69 (m, 2H), 7.29–7.32 (m, 1H), 7.47 (d, J = 9.0 Hz, 1H), 7.65 (d, J = 3.0 Hz, 1H), 7.78 (d, J = 9.0 Hz, 2H). EI-MS m/z 355 (M^+).

2.1.25. 6-(2-(2-(2-Hydroxy-ethoxy)-ethoxy)ethoxy)-4′-methylaminoflavone (16c)

The same reaction as described above to prepare **13** was used, and 145 mg of **16c** was obtained from **14c** in a yield of 64.8%. ^{1}H NMR ($CDCl_3$) δ: 2.92 (d, J = 3.0 Hz, 3H), 3.63 (t, J = 5.4 Hz, 2H) 3.72–3.76 (m, 6H), 3.91 (t, J = 5.1 Hz, 2H), 4.25 (t, J = 4.8 Hz, 3H), 6.65 (s, 1H), 6.68 (s, 2H), 7.28–7.32 (m, 1H), 7.46 (d, J = 9.3 Hz, 1H), 7.59 (d, J = 2.2 Hz, 1H), 7.77 (d, J = 8.7 Hz, 2H).

2.1.26. 6-(2-(2-Fluoro-ethoxy)-ethoxy)-4′-methylaminoflavone (17b)

The same reaction as described above to prepare **8** was used, and 9 mg of **17b** was obtained from **16b** in a yield of 21.9%. ^{1}H NMR ($CDCl_3$) δ: 2.93 (d, J = 5.1 Hz, 3H), 3.79 (t, J = 4.2 Hz, 1H), 3.85–3.95 (m, 3H), 4.26 (t, J = 4.8 Hz, 3H), 4.53 (t, J = 4.2 Hz, 1H), 4.70 (t, J = 4.5 Hz, 1H), 6.65 (s, 1H), 6.68 (s, 2H), 7.28–7.32 (m, 1H), 7.47 (d, J = 9.0 Hz, 1H), 7.59 (d, J = 3.0 Hz, 1H), 7.78 (d, J = 9.0 Hz, 2H). EI-MS m/z 357 (M^+).

2.1.27. 6-(2-(2-(2-Fluoro-ethoxy)-ethoxy)ethoxy)-4′-methylaminoflavone (17c)

The same reaction as described above to prepare **8** was used, and 20 mg of **17c** was obtained from **16c** in a yield of 13.8%. ^{1}H NMR ($CDCl_3$) δ: 2.92 (d, J = 4.8 Hz, 3H), 3.69–3.76 (m, 5H), 3.82 (t, J = 4.5 Hz, 1H), 3.91 (t, J = 4.8 Hz, 2H), 4.25 (t, J = 4.2 Hz, 3H), 4.50 (t, J = 4.2 Hz, 1H), 4.66 (t, J = 4.5 Hz, 1H), 6.65 (s, 1H), 6.68 (s, 2H), 7.28–7.31 (m, 1H), 7.46 (d, J = 9.3 Hz, 1H), 7.59 (d, J = 3.0 Hz, 1H), 7.77 (d, J = 8.7 Hz, 2H). EI-MS m/z 401 (M^+).

2.1.28. 4-Nitrobenzoic acid 2-acetyl-4-fluorophenyl ester (18)

The same reaction as described above to prepare **1** was used, and 2.5 g of **18** was obtained from 2-hydroxy-5-fluoroacetophenone and 4-nitrobenzoyl chloride in a yield of 85.6%. ^{1}H NMR (300 MHz, $CDCl_3$) δ: 2.56 (s, 3H), 7.23–7.34 (m, 2H), 7.56–7.60 (m, 1H), 8.37 (s, 4H).

2.1.29. 1-(5-Fluoro-2-hydroxyphenyl)-3-(4-nitrophenyl)propane-1,3-dione (19)

The same reaction as described above to prepare **2** was used, and 2.5 g of **19** was obtained from **18** in a yield of 96.3%. ^{1}H NMR (300 MHz, $CDCl_3$) δ: 6.81 (s, 2H), 7.02 (d, J = 9.0 Hz, 1H), 7.45 (d, J = 9.0 Hz, 1H), 7.68 (s, 1H), 8.11 (d, J = 8.7 Hz, 2H), 8.36 (d, J = 8.7 Hz, 2H), 11.7 (s, 1H).

2.1.30. 6-Fluoro-4′-nitroflavone (20)

The same reaction as described above to prepare **3** was used, and 2.0 g of **20** was obtained from **19** in a yield of 85.3%. EI-MS m/z 285 (M^+).

2.1.31. 6-Fluoro-4′-aminoflavone (21)

The same reaction as described above to prepare **4** was used, and 944 mg of **21** was obtained from **20** in a yield of 67.4%. ^{1}H NMR (300 MHz, $CDCl_3$) δ: 4.13 (s, broad, 2H), 6.74 (s, 1H), 6.76 (d, J = 9.0 Hz, 2H), 7.35–7.42 (m, 1H), 7.51–7.56 (m, 1H), 7.75 (d, J = 8.7 Hz, 2H), 7.82–7.85 (m, 1H).

2.1.32. 6-Fluoro-4′-methylaminoflavone (22)

To a mixture of **21** (300 mg, 1.2 mmol) and paraformaldehyde (179 mg, 5.9 mmol) in MeOH (15 mL) was added a solution of NaOMe (0.34 mL, 28 wt % in MeOH) dropwise at 0 °C. The mixture was stirred under reflux for 1 h. After addition of $NaBH_4$ (246 mg, 6.5 mmol), the solution was heated under reflux for 45 min. To the cold mixture, 1 M NaOH was added followed by extraction with $CHCl_3$. The organic phase was dried over Na_2SO_4 and filtered. The solvent was removed, and the residue was purified by silica gel chromatography (hexane/ethyl acetate = 5:3) to give 314 mg of **22** (99.2%). ^{1}H NMR (300 MHz, $CDCl_3$) δ: 2.91 (s, 3H), 4.37 (s, broad, 1H), 6.63 (s, 1H), 6.66 (s, 2H), 7.32–7.39 (m, 1H), 7.49–7.53 (m, 1H), 7.74 (d, J = 8.7 Hz, 2H), 7.82–7.85 (m, 1H).

2.1.33. 6-Fluoro-4′-dimethylaminoflavone (23)

The same reaction as described above to prepare **5** was used, and 203 mg of **23** was obtained from **21** in a yield of 61.0%. ^{1}H NMR (300 MHz, $CDCl_3$) δ: 3.08 (s, 6H), 6.69 (s, 1H), 6.76 (d, J = 9.3 Hz, 2H), 7.35–7.41 (m, 1H), 7.51–7.56 (m, 1H), 7.81 (d, J = 9.0 Hz, 2H), 7.83–7.86 (m, 1H).

2.1.34. 6-(2-Tosyloxyethoxy)-4′-dimethylaminoflavone (24a)

To a solution of **8a** (136 mg, 0.28 mmol) in pyridine (4 mL) was added tosyl chloride (122 mg, 0.65 mmol) in an ice bath. The reaction mixture was stirred for 32 h at room temperature following the reaction in an ice bath for 1 h. The organic phase was dried over Na_2SO_4 and filtered. The solvent was removed, and the residue was purified by silica gel chromatography (chloroform/MeOH = 20:1) to give 50 mg of **24a** (36.8%). ^{1}H NMR (300 MHz, $CDCl_3$) δ: 2.45 (s, 3H), 3.07 (s, 6H), 4.23 (t, 2H, J = 4.5 Hz), 4.41 (t, J = 5.1 Hz, 2H), 6.68 (s, 1H), 6.75 (d, J = 9.0 Hz, 2H), 7.12–7.18 (m, 1H), 7.35 (d, J = 8.1 Hz, 2H), 7.43–7.56 (m, 2H), 7.82 (t, J = 9.0 Hz, 4H). EI-MS: m/z 479 [M^+].

2.1.35. 6-(2-(2-Tosyloxyethoxy)ethoxy)-4′-dimethylaminoflavone (24b)

The same reaction as described above to prepare **24a** was used, and 111 mg of **24b** was obtained from **8b** in a yield of 34.1%. ^{1}H NMR (300 MHz, $CDCl_3$) δ: 2.41 (s, 3H), 3.08 (s, 6H), 3.76–3.85 (m, 4H), 4.12 (t, J = 5.1 Hz, 2H), 4.22 (t, J = 5.1 Hz, 2H), 6.70 (s, 1H), 6.76 (d, J = 9.0 Hz, 2H), 7.25–7.33 (m, 3H), 7.47 (d, J = 9.0 Hz, 1H), 7.55 (d, J = 3.0 Hz, 1H), 7.79–7.83 (m, 4H). EI-MS m/z 523 (M^+).

2.1.36. 6-(2-(2-(2-Tosyloxyethoxy)ethoxy)ethoxy)-4′-dimethylaminoflavone (24c)

The same reaction as described above to prepare **24a** was used, and 35 mg of **24c** was obtained from **8c** in a yield of 39.9%. ^{1}H NMR (300 MHz, $CDCl_3$) δ: 2.43 (s, 3H), 3.08 (s, 6H), 3.62–3.73 (m, 6H), 3.87 (t, J = 4.8 Hz, 2H), 4.16–4.21 (m, 4H), 6.70 (s, 1H), 6.76 (d, J = 9.0 Hz, 2H), 7.28–7.33 (m, 3H), 7.47 (d, J = 9.0 Hz, 1H), 7.60 (d, J = 2.2 Hz, 1H), 7.79–7.83 (m, 4H). EI-MS m/z 567 (M^+).

Please cite this article in press as: Ono, M. et al., *Bioorg. Med. Chem.* (2009), doi:10.1016/j.bmc.2009.01.025

2.2. Radiolabeling

[^{18}F]Fluoride produced by an ultracompact cyclotron (CYPRIS model 325R; Sumitomo Heavy Industry Ltd) via an $^{18}O(p,n)^{18}F$ reaction was adsorbed to a strong-base anion exchange resin (Bio-Rad), and was eluted with 500 μL of K_2CO_3 solution (33 mM) into 1 mL of acetonitrile containing Kryptofix 222 (K222) (20 mg). The solvent was removed azeotropically with anhydrous acetonitrile at 120 °C under a nitrogen stream. A solution of tosylate precursor **24(a–c)** (0.2 mg) in 400 μL of DMSO was added to the reaction vessel containing [^{18}F]Fluoride. The mixture was heated at 160 °C for 5 min. The reaction mixture was purified by the reversed phase HPLC system (a Shimadzu LC-6A isocratic pump, a Shimadzu SPD-6A UV detector and an Aloka NDW-351D scitillation detector) on a YMC Hydrosphere C18 column (20 × 150 mm) with acetonitrile/water (70:30) at a flow rate of 9.0 mL/min to obtain [^{18}F]**8(a–c)**. The radiochemical purity and specific activity were determined by analytical HPLC on a YMC Pack Pro C18 column (4.6 × 150 mm, acetonitrile/water (60:40), 1.0 mL/min).

2.3. Binding assays using the aggregated Aβ peptide in solution

A solid form of Aβ(1-42) was purchased from Peptide Institute (Osaka, Japan). Aggregation of peptides was carried out by gently dissolving the peptide (0.25 mg/mL) in a buffer solution (pH 7.4) containing 10 mM sodium phosphate and 1 mM EDTA. The solutions were incubated at 37 °C for 42 h with gentle and constant

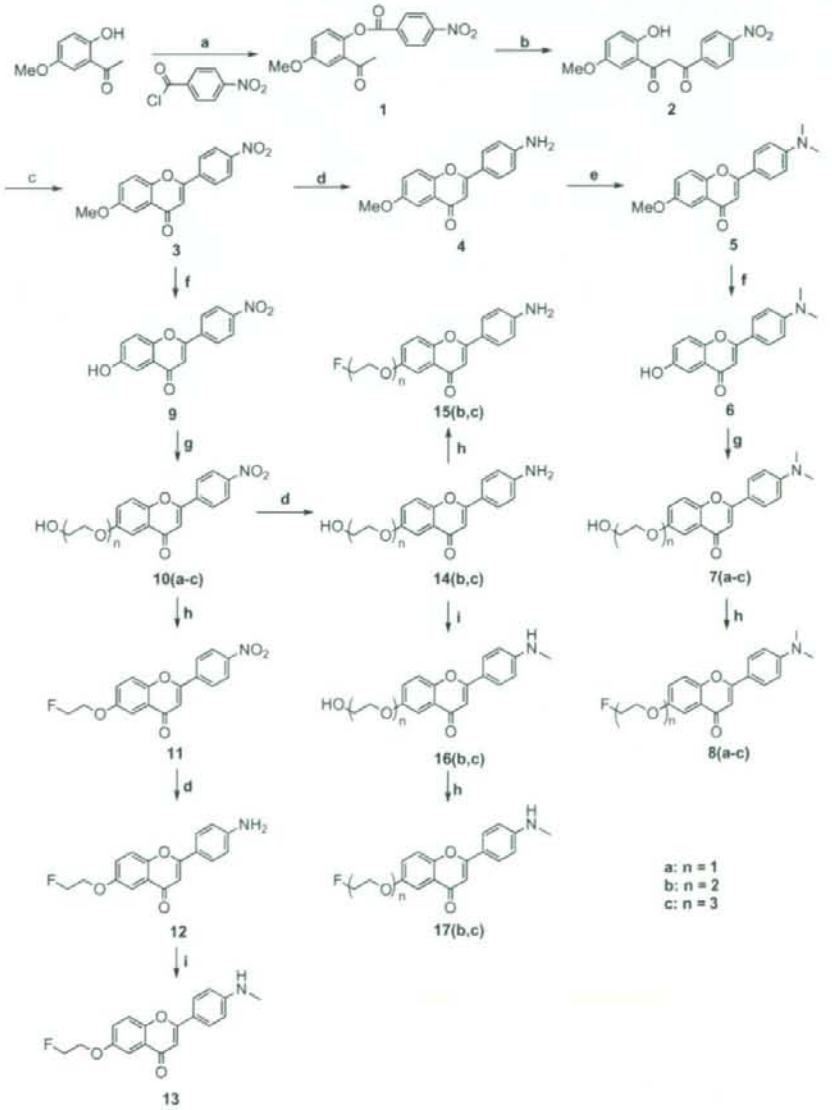

Scheme 1. Reagents: (a) pyridine; (b) KOH, pyridine; (c) H_2SO_4, AcOH; (d) EtOH, $SnCl_2$; (e) $(CH_2O)_n$, $NaCNBH_3$, AcOH; (f) CH_2Cl_2, BBr_3; (g) Cl-(-O-)$_n$-H (n = 1–3) K_2CO_3, DMF; (h) DAST, DME; (i) DMSO, CH_3I, K_2CO_3.

Please cite this article in press as: Ono, M. et al., *Bioorg. Med. Chem.* (2009), doi:10.1016/j.bmc.2009.01.025